University of Northern Colorado
Scholarship & Creative Works @ Digital UNC

Master's Theses | Student Research

8-2019

Comparing Terrestrial and Extraterrestrial Lava Surface Roughness Using Digital Elevation Models From High Resolution Topography and Structure From Motion

Davitia Hannah James
davitiaj@gmail.com

Follow this and additional works at: https://digscholarship.unco.edu/theses

Recommended Citation

James, Davitia Hannah, "Comparing Terrestrial and Extraterrestrial Lava Surface Roughness Using Digital Elevation Models From High Resolution Topography and Structure From Motion" (2019). *Master's Theses*. 94.
https://digscholarship.unco.edu/theses/94

This Text is brought to you for free and open access by the Student Research at Scholarship & Creative Works @ Digital UNC. It has been accepted for inclusion in Master's Theses by an authorized administrator of Scholarship & Creative Works @ Digital UNC. For more information, please contact Jane.Monson@unco.edu.

© 2019

DAVITIA JAMES

ALL RIGHTS RESERVED

UNIVERSITY OF NORTHERN COLORADO

Greeley, Colorado

The Graduate School

COMPARING TERRESTRIAL AND EXTRATERRESTRIAL LAVA SURFACE ROUGHNESS USING DIGITAL ELEVATION MODELS FROM HIGH RESOLUTION TOPOGRAPHY AND STRUCTURE FROM MOTION

A Thesis Submitted in Partial Fulfillment
of the Requirements for the Degree of
Master of Arts

Davitia James

College of Natural and Health Sciences
Earth and Atmospheric Sciences
Earth Science

August 2019

This Thesis by: Davitia James

Entitled: *Comparing Terrestrial and Extraterrestrial Lava Surface Roughness Using Digital Elevation Models from High Resolution Topography and Structure from Motion*

has been approved as meeting the requirement for the Degree of Master of Arts in College of Natural and Health Sciences in Department of Earth and Atmospheric Sciences, Program of Geology.

Accepted by the Thesis Committee:

_____
Steven W. Anderson, Ph.D., Chair

_____
Sharon Bywater-Reyes, Ph.D., Committee Member

_____
William Hoyt, Ph.D., Committee Member

Accepted by the Graduate School

_____
Linda L. Black, Ed.D.
Associate Provost and Dean
Graduate School and International Admissions
Research and Sponsored Projects

ABSTRACT

James, Davitia. *Comparing Terrestrial and Extraterrestrial Lava Surface Roughness Using Digital Elevation Models from High Resolution Topography and Structure from Motion*. Unpublished Master of Arts thesis, University of Northern Colorado, 2019.

If patterns of lava flow surface roughness at large and small scales can be tied features at similar scales using observations of active volcanoes, then roughness across a lava flow can be related to eruption characteristics such as rate of flow, viscosity, and underlying slope. This will further current understanding of emplacement rates and styles during the volcanically active period of mars' history. Additionally, describing the effect of the Martian environment on volcanism is necessary to learn the full range of possible volcanic activity in the Solar System. This will also provide insight regarding volcanic hazards here on Earth. To investigate lava flow roughness on Earth and Mars, I acquired high resolution topography for lava flows from Mauna Ulu, Hawaii, Obsidian Dome and Amboy, California using Structure from Motion and/or LiDAR, as well as topography data of Tharsis from the HiRISE camera on the Mars Reconnaissance Orbiter. Mauna Ulu and Amboy were used as earthly analogues for the range of possible lava flow surfaces on mars. I applied two new approaches to determining roughness on lava flows – the Topographic Position Index and Roughness Doughnut. The approaches presented here may allow scientists to observe much finer features in flow fields than previously possible, thus providing new insights about the quantitative relationships between surface morphology and eruption characteristics. Finally, I used Principal Component Analysis to better understand the relationships between terrestrial and martian roughness.

The goal of this project was to develop an efficient and cost-effective method of roughness comparison that can be applied to a variety of volcanic environments and scales. Mauna Ulu offers an opportunity to observe young flows, but the dominant weathering processes in this humid, tropical location are significantly different from processes active on Mars. Lava flows at Amboy are older than those produced by Mauna Ulu, and display varying levels of mantling by wind-blown sand, similar to expectations of Mars. Using datasets from both locations, I described how martian lava flows compare to the range of roughness measurements at both terrestrial sites. I also sought to investigate the effect of mantling of aeolian material on lava flow roughness, and if roughness is a useful tool to detect mantled lava flow features on Mars. Additionally, I aimed to relate roughness data from the terrestrial locations to lava flow features visible in Structure from Motion and LiDAR digital elevation models. Finally, I discuss the use of these methods to map volcanic features and environments in new locations on Earth and on Mars. Though Obsidian Dome was not a central part of this project, 1 meter per pixel LiDAR data was used to illustrate the roughness differences between silicic and mafic lava flows. Roughness values are higher at Obsidian Dome than values at the other locations, at every scale tested. This is consistent with observations by Plaut et al. (2004).

Results show that suspected basaltic lava flows on Mars show similarities to the range of roughness values for basaltic flows at Amboy, California and Mauna Ulu, Hawaii. Roughness values for the basaltic environments are significantly different from those of Obsidian Dome. I was able to use roughness of lava flows within and outside of the main wind shadow at Amboy to describe the effect of mantling on the lava topography. Though a roughness trend was observed across mantled surfaces in

California, it is not robust enough to be used as the only method to detect mantled lava flows on Mars. Finally, both the RD and TPI methods can be used to map volcanic environments but would benefit from additional datasets.

ACKNOWLEDGEMENTS

This project has offered me so many amazing experiences and opportunities for growth over the last two years. The trip to Hawaii was filled with moments I will talk about for the rest of my life! Thank you Dr. Anderson for the opportunity to visit Kilauea, as well as for your guidance, advice and for believing in me and my ideas during this project. Thank you to Dr. Hoyt and Dr. Bywater-Reyes for always being willing to answer questions and reviewing an endless stream of drafts! I am grateful for your patience and suggestions.

Thank you to my family and friends for being so supportive! I would have never made it this far without your encouragement, phone calls and prayers. I could feel you with me every step of the way despite being separated by thousands of miles. In particular I have to thank my mother for everything. Zoie and Irene, your care packages helped more than you will ever know. Alex and Sio, thank you for the emotional support at all hours of the day and night, and for celebrating every little milestone with me.

Research and travel costs for this project were covered by grants from University of Northern Colorado College of Natural and Health Sciences, the Graduate Student Association, and the Earth and Atmospheric Science Department. The Career Development Award from the Lunar and Planetary Science Institute allowed me travel to Houston to present my results at the 2019 Lunar and Planetary Science Conference.

TABLE OF CONTENTS

LIST OF TABLES

LIST OF FIGURES

CHAPTER I

INTRODUCTION

Identification of lava flows on Mars can further understanding of the geologic history of the planet by confirming the styles, timing, and geographic extent of volcanic activity that occurred. However, using only the planform shape observed in visible light images to identify these features is typically not diagnostic. For example, a lobate feature located on a slope cannot simply be called a lava flow as this shape in this setting may be a result of a variety volcanic and non-volcanic processes. Landslides and rock glaciers share the lobate appearance of pyroclastic flows, lahars, and lava flows. Despite similar planform appearances, each of these features have different roughness signatures that can be linked to their different origins. This concept is the foundation of my thesis research. Previous work (Plaut et al., 1994; Anderson et al., 1998; Shepard et al., 2001; Plaut et al., 2002) evaluated lava roughness and concluded that some flows can be distinguished by roughness. Plaut and others (2002) found that silicic flows are much rougher at every scale than basalt flows. Differentiating other volcanic products using roughness is more complex. My assumption was that roughness patterns in addition to roughness values across a lava flow surface may be useful for this.

Shepard and others (2001) defined surface roughness as the "topographic expression of surfaces at horizontal scales of millimeters to a few hundred meters". The stories of some volcanic eruptions are told through the variations in lava flow roughness at different scales. Consider ropey folds preserved on the surface of a pahoehoe flow

(Fink, 1980). Though the rippled features may appear flat and devoid of height changes at the meter and decameter scale, the texture is quite rough when observed at the centimeter scale (Figure 1a). We know that these folds are indicative of slowly moving, low viscosity pahoehoe flows because of observations of terrestrial basaltic volcanic eruptions (Byrnes et al., 2001; Byrnes et al., 2004; Swanson, 1973; Moore et al., 1975). Tumuli also provide an example of relating roughness to emplacement conditions (Figure 1b) (Fink and Anderson, 2000; Anderson et al., 2012). These inflation features resemble the back of a whale and are smooth at smaller, centimeter scales but always display significant roughness at scales half a meter to tens of meters. Tumuli and folds are both different from a'a' lava flows, which are composed of piles of jagged blocks and are rough at centimeter to decameter scale (Figures 1c and 1d) (Peterson and Tilling, 1980; Gaddis et al., 1990; Farr, 1992; Shepard et al., 2001; Diniega et al., 2018). Table 1 shows lava surface features and the scales at which they are observed.

Table 1: Features Affecting Lava Flow Roughness at Different Scales

	Small scale	Medium scale		Large scale
	Millimeter to Centimeter	Centimeter to meter	Meter	Decameter and larger
Dominant features at this scale	Gas bubble walls and minor folds and cracks	Flow toes and blocks	Tumuli, ridges and crease patterns	Full flow fields, sheeted flows and levees
Common techniques for assessing roughness	RMS slope and height, stylus profiles	RMS slope and height, laser and stylus profiles	Laser profiles, RMS slope and height	Radar, elevation standard deviation, RMS slope and height
Minimum resolution required	<1 m	<1 m	~1 m	>5 m

Figure 1a (upper left): Ropey pahoehoe folds showing cm-scale roughness. Photo: Author.
Figure 1b (upper right): Tumulus in a flow field showing meter to decameter-scale roughness. Photo: Author.
Figure 1c (lower left): A'a' lava over pahoehoe. Note the contrasting cm-scale roughness. Photo: S.W. Anderson.
Figure 1d (lower right): Active a 'a' lava flowing older pahoehoe. Note the blocky texture of the flow front. Photo: Smithsonian Institution Global Volcanism Program.

Roughness has been quantified using multiple methods including radar scatter (Farr and Engheta, 1983; Evans et al., 1992; Campbell and Shepard, 1996; Greeley et al., 1998), profile lengths measured by hand and with lasers (Brown and Scholz, 1985; Chapman, 1985), standard deviation of elevation (Whelley et al., 2011), root mean square height and slope (Campbell and Shepard, 1996; Tian et al., 2011) as well as ground-based and airborne stereo-photography (McCue and Green, 1965; Farr, 1992). As sand and dust settle over volcanic landforms, this deposition limits our confidence in interpreting visual and topographic data in the volcanic regions of Mars. Common techniques for describing roughness are variable across locations and are limited in their usefulness as descriptive

measures of a surface. Additionally, previous studies have not sufficiently accounted for the effect of mantling on roughness. Hence the necessity of this project.

In this thesis I evaluated two new approaches to lava surface roughness – the Topographic Position Index, and Roughness Doughnut – on three terrestrial analogue sites and several suspected lava flows on Mars. The terrestrial locations are Mauna Ulu in Hawaii, Amboy Crater and flow field in California, and Obsidian Dome in California. Lava flows from the most recent eruptions of Mauna Ulu and Amboy were used as terrestrial analogues for the range of possible lava flow surfaces on Mars. Both are basaltic volcanoes, and have similar surface features to flows in the Tharsis region of Mars (Byrnes and Crown, 2004; Glaze et al., 2005, Greeley and Bunch, 1976). Mauna Ulu offers an opportunity to observe young flows, although the dominant weathering processes in this humid, tropical location are significantly different from processes active on Mars (Byrnes et al, 2004). Amboy Crater ties both sites together. Lava flows at Amboy are older than those produced by Mauna Ulu, and are located in the Mojave Desert so there are varying levels of mantling by wind-blown sand in dry conditions similar to what is observed at Tharsis. Plaut and others (1993) showed that silicic domes in the Inyo Chain of eastern California's Long Valley Caldera are among the roughest naturally occurring surfaces ever measured, at every scale. For this reason, Obsidian Dome, one of three rhyolitic feature analyzed by Plaut and others (1994), was included as an additional dataset in this research. Surface roughness values of Obsidian Dome provide a highly valuable comparison to roughness values of Mauna Ulu, Amboy and Tharsis.

Basaltic lava generally produces effusive eruptions due to low viscosity and high magma temperatures, though sudden contact with colder material can result in explosions near the surface (Bonatti and Harrison, 1988; Cervantes and Wallace, 2003). Explosive basaltic eruptions are also linked to confining pressure from overlying rock or the atmosphere which induces rapid expansion of molten material (Parfitt, 2004). The lava produced by explosive eruptions are frothy and much rougher at small scales (many bubbles and tiny cracks) compared to those produced by effusive activity (more likely to have denser, glassy, ropy surfaces). As a lava flow travels downslope, increased flow speed causes it to fold or break into blocks if the surface is steeply sloping due to the flow front stagnating from cooling (Anderson et al., 1998; Guest et al., 2011). This will affect centimeter to decameter-scale roughness. If the underlying surface is flat, the flow will advance slowly and have more time to cool, producing a smooth crust while intact, and a rougher surface if the crust breaks into blocks (Figure 1d) (Anderson et al., 1998). Additionally, a high rate of magma effusion causes transition to blocky a'a' flows which are rougher than pahoehoe (Peterson and Tilling, 1980; Kilburn, 1981; Cervantes and Wallace, 2003). Thus, lava morphology reflects the characteristics and eruption history of the volcano that produced the flow.

If roughness can be used to identify lava flow features, and if these features reflect eruption conditions, then using patterns of roughness across a lava flow may later be tied to emplacement conditions such as rate of flow, viscosity, and underlying slope (Fink and Anderson, 2000; Anderson and Fink, 1989; Anderson and Fink, 1992; Anderson et al., 1995; Anderson et al., 1998; Mallonee et al., 2017; Guest et al., 2011; Fink and Grifiths, 1998; Peterson and Tilling, 1980; Long and Wood, 1986; Swanson,

1973) this allows the use of high-resolution topographic datasets to interpret volcanic eruptions. This is particularly important in planetary settings when topography data is typically more abundant, and higher resolution than visible light images.

The central goal of this project was to develop an effective method of quantitatively comparing morphological features on terrestrial and extraterrestrial lava flows from their roughness characteristics. With high-resolution topographic data sets of Mars available from the High Resolution Imaging Science Experiment (HiRISE) and Context (CTX) cameras aboard the Mars Reconnaissance Orbiter, scientists are now able to detect medium-scale features (~1m on the ground) such as tumuli, ridges, and large folds that previously were not clearly visible in older, lower resolution datasets. Although recent missions have provided imagery capable of detecting lava flow features as small as a few meters (Theilig and Greeley, 1986), image interpretation does not always provide an unambiguous interpretation regarding the identity of a feature on another planet. For this reason more quantitative approaches may be needed to positively identify lava flow surface structures. High resolution topographic dataset such as Mars Orbiter Laser Altimeter (MOLA) and HiRISE typically have even better resolution than visible imagery – up to 0.3 meters per pixel. Improved resolution allows for new quantitative approaches such as roughness analysis to interpret volcanic surfaces. This offers a path to answering fundamental questions about emplacement rates and styles of volcanism on Mars. Detailing the true effect of the environment on volcanism (such as differences in gravity and atmospheric pressure) will further our understanding of the full range of possible volcanic activity, as well as provide insight regarding volcanism and associated hazards here on Earth.

Hawaii's pristine flows that have not yet experienced any significant erosion provide roughness values of fresh lava surfaces, whereas Amboy's older lava flows are partially covered by sand and yield roughness values of partially weathered and mantled surfaces that are believed to be morphologically similar to flows on Mars (Huges et al., 2019; Greeley and Bunch, 1976). Using datasets from all three locations, this research project aimed to answer the following questions:

Q1 Can roughness data from terrestrial locations be confidently related to lava flow features using Structure from Motion and LiDAR DEMs?

Q2 Do martian lava flows fit into the range of observations from both terrestrial analogue sites based on roughness?

Q3 What is the effect of wind mantling on roughness of large- and small-scale terrestrial lava flow features and can roughness help us detect mantled lava flow features on Mars?

Q4 Can roughness reliably map volcanic features and environments on both Earth and Mars?

The techniques presented here may allow scientists to positively detect much finer features in flow fields than previously possible, thus providing new insights about the quantitative relationships between surface morphology and eruption characteristics.

CHAPTER II

PROJECT BACKGROUND

2.1 Previous Studies of Lava Flow Roughness

As described in the previous chapter, there is a wide range of research on surface roughness, as well as a variety of methods that can be used to quantify roughness. Measurements of lava flow surface roughness on Earth are used to describe changes in eruption conditions across a flow (Swanson, 1973; Kilburn, 1981; Greeley and Martel, 1988), surface processes that have occurred post-emplacement (Wells et al., 1985; Shepard et al., 2001), and to map flow units (Gaddis et al., 1990; Morris et al., 2008). The relationship between lava roughness and composition has been explored by scientists investigating of basaltic lava flows (Farr, 1992; Moncrief and Rowland, 1991; Evans et al., 1992) and silicic flows (Anderson et al., 1998; Ramsey and Fink, 1999; Plaut et al., 2002).

The roughness of lava flows is a key focus of planetary research, and is particularly important to comparative studies of volcanism throughout the solar system. Planetary surface roughness is crucial to geologic mapping (Kreslavsky and Head, 2000), determining the suitability of potential landing sites (Golombek et al., 1997; Simurda 2018), and constraining emplacement dates and extent of volcanic activity (Lopes and Kilburn 1990; McSween et al., 2003). The most common targets of planetary studies of lava flow roughness are Venus (Theilig et al., 1988; Head et al., 1992; Plaut et al., 1994; Stofan et al 2000; Byrnes and Crown, 2002) and Mars (Garneau and Plaut, 2000;

Keszthelyi et al., 2000; Giacomini et al., 2009; Crown et al., 2015; Mallonee et al., 2017a; Mallonee et al., 2017b; Tolometti et al., 2017; Hamilton et al., 2018; Zanetti et al., 2018; Huges et al., 2019).

2.2 Geologic Settings

Since Amboy, Mauna Ulu and Tharsis are all characterized by mafic compositions, differences in flow morphology are a result of local emplacement conditions such as underlying topography, cooling rate, emplacement rate, and extrusion style, as well as by global constants like gravity and atmospheric pressure (Guest et al., 1987; Lopes and Kilburn, 1990; Byrnes and Crown, 2002; Diniega et al., 2018). These sites vary in age, amount of erosion, and their degree of mantling by aeolian deposits, as summarized in Table 2.

Table 2: Differences in flow morphology and emplacement styles at the terrestrial analogue sites

	Mauna Ulu, Hawaii	Amboy, California	Tharsis, Mars
Flow morphologies	Proximal 1: dense, thin, vesicular flows. Proximal 2: shelly, buckley, warped flows. Distal: inflated, hummocky, glassy flows.	Proximal: smooth, dense, flat surfaced flows. Proximal: inflated, fractured flows.	Varied
Emplacement conditions	Lava fountaining, vent overflows, lava tubes.	Slow moving, inflated vent lavas.	Varied
Suitability as martian analogue	Proposed similarities in morphology to young lava flows on Mars, as well as those in areas with a low dust index.	Older lava flows affected by erosional processes similar to those on Mars.	-

2.2.1 Mauna Ulu, Hawaii

Mauna Ulu is a small Hawaiian shield volcano (Figure 2) along Kilauea's East Rift Zone and was last active from 1969-1974 (Swanson, 1973). During this period, it displayed a variety of eruption styles and produced an extensive (~62 km^2) flow field (Byrnes et al., 2004; Moncrief and Rowland, 1991). This field is composed of multiple overlapping, compound flow units of differing age and emplacement style (Figure 3). Small- and large-scale roughness elements are present, enabling researchers to link morphology to emplacement conditions. These flows have also been studied as a terrestrial analogue for martian lavas (Byrnes et al., 2004). Specific conditions known to affect morphology in this flow field are rates of effusion and inflation, mechanisms of lava transport, storage and distribution, flow rheology, degassing and topography.

Figure 2: Google Earth Satellite photo showing the Mauna Ulu volcano (red circle), Mauna Ulu field site (yellow pin), lava flowing over the Pali (fault scarp).

Figure 3: Photo taken from the Hawaii field site facing the Pali (fault scarp). Overlapping flows from the 1974 Mauna Ulu eruption are visible. Darker flows are rougher a'a' flows overlying the smoother pahoehoe. Photo by author. The car is approximately 4 meters long.

Variations in these conditions have produced three pahoehoe morphologies at Mauna Ulu. The distinctions between each morphology are not sharp, instead there are gradual transitions between the types (Swanson, 1973). Swanson (1973) first described two pahoehoe morphologies found primarily in areas proximal to the vent. The first is characterized by a smooth surface. This type is dense and thin with minimal vesicles as it formed from lava fountaining where most of the gas was released during eruption (Swanson, 1973; Byrnes et al., 2004). A second type of near-vent pahoehoe is produced by lava overflowing from the vent with higher gas content and are more likely to buckle and display a shelly, vesicular texture (Swanson, 1973). The third type is commonly found in the distal reaches of the flow field and is delivered via lava tube systems (Swanson, 1973). Lavas still had a relatively high gas content when emplaced. As a result, these lavas have an inflated, hummocky topography and multiple gas cavities. They are highly lobate with glassy surfaces and tumuli are a significant feature (Byrnes et

al., 2004). This inflated morphology dominated our chosen field site for this project and is morphologically similar to flows mapped in the Tharsis region of Mars (Theilig and Greeley, 1986). If relationships exist between roughness variables and emplacement characteristics at Mauna Ulu, they could provide insight into flow field development in this area, as well as eruptive processes occurring in other, more remote, and planetary locations. The Mauna Ulu flows are essentially unweathered and unmantled at the scale of our study.

2.2.2 Amboy, California

Amboy Crater is an extinct, ~79,000-year-old cinder cone and flow field in the eastern Mojave Desert (Phillips, 2003) that has also been used as a martian analogue by several researchers (Greeley and Bunch, 1976; Finnegan et al., 2004; Kienenberger and Greeley, 2012). The Amboy lava field surrounds the crater and covers an approximately 70 km^2 area between the Bullion Mountains to the west and the Bristol Mountains to the east. (Chesterman et al., 1971; Finnegan et al., 2004). These mountains provide a steady supply of sand-sized sediment and wind direction is predominantly south-east based on prominent wind streaks visible in aerial photography (Figure 4). The Amboy crater and flow field are the southernmost features in a NW chain of alkali-basalt volcanic centers from the Pliocene-Pleistocene Periods (Greeley and Bunch, 1976; Phillips, 2003). Eruptions at Amboy produced pahoehoe flows of alkali basalts that are chemically similar to ocean island basalts. Variations in elemental and isotopic concentrations indicate that melts of pure mantle were contaminated by mafic crust (Glazner et al., 1991). Volcanism in the Mojave Desert is a result of tectonic activity in the Neogene that caused crustal extension and thinning (Garfunkel, 1974).

Figure 4: Google Earth Satellite image showing the Amboy Crater, the distinct wind streaks extending south east, and field sites marked by the yellow pins.

Figure 5: View of Amboy Crater and surrounding sand covered lava flows. Photo by author, image oriented to the southwest.

Amboy was last active approximately 10,000 years ago, when it produced hummocky pahoehoe flows with both inflation and deflation features up to 5 meters high (Greeley and Bunch, 1976). Tumuli and pressure ridges are abundant across the flow, as are a small number of lava channels. The basalt at this site is primarily dense, but some

vesicular units are present (Greeley and Bunch, 1976). Circular pits linked to collapse of the plastic crust around a single point mark the oldest lava flows in the southeastern and eastern area of the lava field. Assessments by Greeley and Bunch (1976) confirmed that these features are approximately 10 meters across and a few meters deep.

Greeley and Bunch (1976) also described two lava flow units that were clearly discernable from aerial photos of the site: platform and vent lavas. The isolated flat, generally smooth basalt surfaces were named platform units and assumed to form from inflation of slow-moving lava. They are 4-5 meters higher than the surrounding sand. Vent lavas were named for their proximity to the field's vents. These are about twice as high as the platform lavas and are fractured around the edges, possibly due to lava draining back to the vent. The surfaces of both units are eroded such that the much of the glassy zone and most of the vesicular zone commonly found on fresh pahoehoe are no long present (Greeley and Bunch, 1976).

Sand does not evenly cover the area – sand thickness ranges from barely a centimeter to over a meter, gathering in the lowest points (Figure 5) (Finnegan et al., 2004). There are several minor wind streaks but the most prominent one extends from the Amboy Crater. These streaks are areas where the wind is blocked by the elevated edge of another feature, and the underlying lava is exposed as dark streaks (Greeley and Bunch, 1976). The main wind streak allows investigation the effect on roughness of varying degrees of mantling at the same site - the locations within the wind streak should be less mantled than those outside it. At the scale of study, lava flows at Amboy are moderately to heavily mantled, and are affected by aeolian and, to a lesser extent, fluvial processes (Byrnes et al., 2007; Kienenberger and Greeley, 2012).

2.2.3 Tharsis, Mars

Though the most recent volcanic eruptions on Mars occurred over 3 billion years ago, previous missions to the planet have found evidence of extensive, even older volcanic activity (Carr and Head, 2010). Volcanic products cover vast areas of the surface, though altered in some places by interactions with water, wind and impacts with other bodies (Werner, 2009). Head et al. (2006) outline the three geologic periods of martian history that have been identified based on widespread surface activity during each time period: the Noachian, Hesperian and Amazonian. Pre-Noachian describes everything from the accumulation and differentiation of the planet to the start of the Noachian period approximately 4.1 to 3.8 billion years ago (Gya). Very little remains of the Pre-Noachian, except for the topographic dichotomy between the northern and southern hemispheres that formed during this period (Carr and Head, 2010). The Noachian was the most active period of martian history and is often referred to as the 'warm, wet Mars' since extensive river systems as well as large lakes existed at the surface and erosion was highest during this period (Craddock and Howard, 2002). The Tharsis region (Figure 6) first became active during the Noachian (Carr and Head, 2010; Head et al., 2006).

When the Hesperian period began approximately 3.7 Gya, hydrologic activity sharply decreased while the cryosphere thickened, and rates volcanism increased globally (Carr and Head, 2010). Massive flood lavas were deposited, and Olympus Mons steadily grew into the largest volcano in the solar system (Carr and Head, 2010). Occasionally, epic floods scoured the planet's surface and temporary lakes and confined seas formed in topographic lows (Carr and Head, 2010; Hamilton et al., 2018; Hauber et al., 2011).

Volcanic activity largely ceased nearly 3.0 Gya when the Hesperian ended. Volcanic activity during the early Amazonian (1.5 Gya to present) was limited to the plains of Tharsis and Elysium in the equatorial regions (Figure 6) (Brož et al., 2017; Crown et al., 2015). Currently, surface processes are related to glaciers, mass wasting and mantling (Carr and Head, 2010).

Contrary to expectations, Hesperian volcanic units are more extensively covered in fine grained sediment than units from the Noachian. Higher rates of mantling for younger units could be explained by more recent pyroclastic events, lower rock strength of Hesperian products and patterns in dust concentration (Rogers and Head, 2017). Although the exact rates of weathering and erosion during martian history are unknown, Greeley and Bunch (1976) suggest that flows at Amboy, California have similar degrees of erosion to older lava flows on Mars (Figure 7). However, younger volcanic units near the planet's shield volcanos and vents should be glassier and more vesicular, similar to Hawaiian pahoehoe (Greeley and Bunch, 1976).

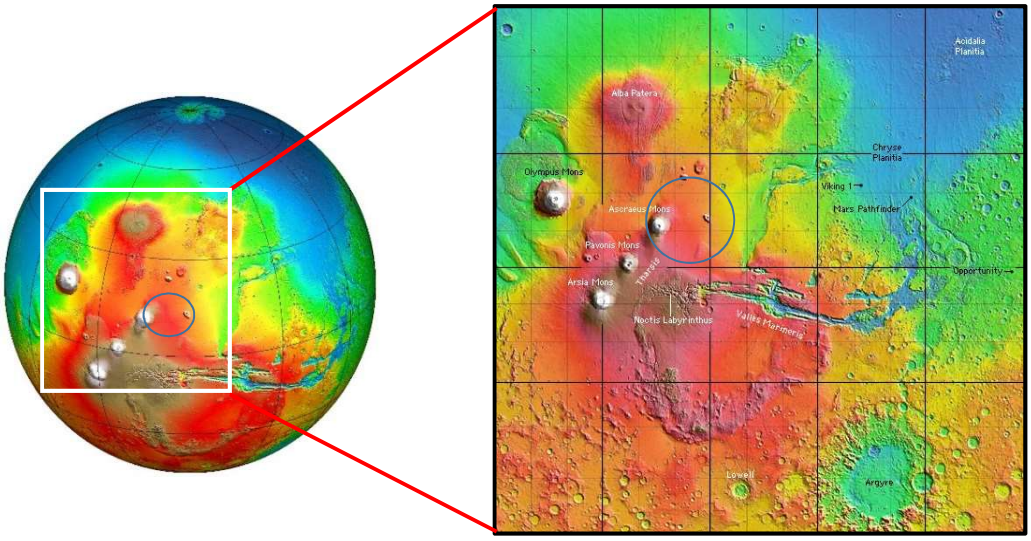

Figure 6: Digital elevation model of the Martian Western Hemisphere highlighting the Tharsis Region in the white box. The area in the blue circle contains the sites studied in this project. HiRISE Image: NASA/JPL/University of Arizona.

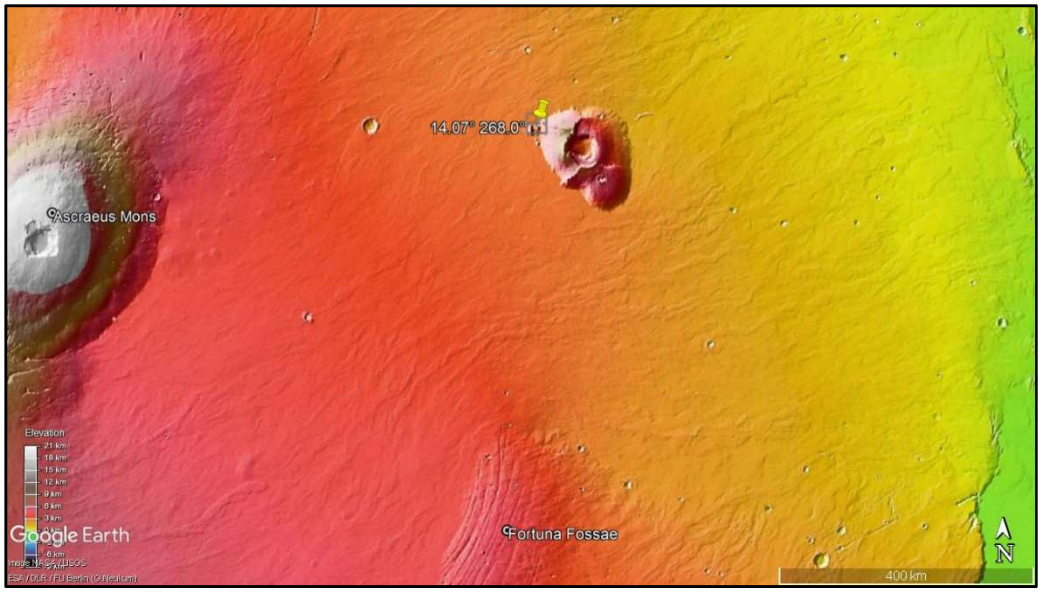

Figure 7: Zoomed in view of the blue circle shown in figure 6: mantled lavas in the Tharsis region of Mars. The location of site used in this study is marked by yellow pin. HiRISE Image: NASA/JPL/University of Arizona.

2.3 Topographic Datasets

2.3.1 Background on Structure from Motion

Stereophotography is the use of photo pairs showing the same feature from different angles to produce overlapping sets of images which, when viewed at the same time, create the illusion of depth. Photogrammetry is the use of photographs to measure distance. Both stereophotography and photogrammetry are central concepts for extracting surface roughness from photo surveys. Both approaches allow researchers to monitor changes in small features on the lava surface that may not be clearly visible in recent Light Detection and Ranging (LiDAR) surveys of the Mauna Ulu and Amboy flow fields. The best currently available LiDAR datasets for each site have a resolution of 1 meter per pixel, but DEMs generated using photogrammetry may have sub-cm scale resolution.

Structure from Motion (SfM) is an affordable answer to the time-consuming and expensive methods of acquiring high resolution topographic data (James and Robson, 2012; Smith et al., 2016). The process of SfM utilizes multiple overlapping photos of a feature of interest to create a dense point cloud and DEM equivalent to those produced by terrestrial and airborne laser scanning systems without consulting experts (Smith et al., 2016; Verma and Bourke, 2018). Additionally, since the only requirement is a hand held Digital Single-Lens Reflex (DSLR) camera, SfM is extremely beneficial to research in the earth sciences as it is not always possible to transport bulky surveying equipment to remote field locations (Micheletti et al., 2015; Westoby et al., 2012). As a result, SfM has recently been applied to numerous and diverse investigations of earth, ocean and atmosphere (Favalli et al., 2012; Westoby et al., 2012; James and Robson, 2014; Javernick et al., 2014; Smith et al., 2016; Bywater-Reyes et al., 2017). Multiple DEMs were produced using Agisoft Photoscan software from 3D recreations of sections of the Amboy and Mauna Ulu sites.

Agisoft PhotoScan is an image-processing software that generates high-quality three-dimensional products that can be further manipulated in Geographic Information System (GIS) software. The process of making a 3D model and DEM requires initiating several automated steps, following an intuitive work flow toolbar (Verma and Bourke, 2018). The creators of Agisoft also provide simple DEM generation tutorials for beginner users in the user manual (Agisoft LLC, 2018). The user first uploads photos to Agisoft, and sorts images to be used in the model based on quality. At this point image markers such a flags and poles should be identified and labelled if any were used. The software then adjusts camera positions for each image and aligns the images to produce a sparse

point cloud. The user must instruct Agisoft to build a dense point cloud using depth and distance data supplied by the cameras. The final steps are creating a polygonal mesh based on the dense point cloud, and draping images over the mesh (referred to as adding texture). Creating a tiled model produces an extremely detailed rendition of the surface but requires a large amount of processing power and time. Due to time restrictions, no tiled models were used in this project. At this point the 3D model can be exported as a DEM for use in other software, saved for later work or used to generate an orthomosaic.

2.3.2 Light Detection and Ranging

Light Detection and Ranging (LiDAR) is a type of active remote sensing that converts elevation data to 3D point clouds, which in turn are used to produce DEMs (Mallet and Bretar, 2009). A laser pulse is emitted from the ground-based or terrestrial scanning system and the distance of an object from the sensor is determined based on the speed and strength of the returning laser beam (Mallet and Bretar, 2009). LiDAR can acquire over 250,000 topographic points per second (Deeb and LeWinter, 2018). LiDAR datasets in this project were acquired from the OpenTopography database and through personal communications. Similar to SfM, LiDAR is valuable for a wide variety of research topics in the earth sciences (Lefsky et al., 1999; Drake et al., 2002; Jutzi et al., 2003; Fidera et al., 2004; Sithole and Vosselman, 2006; Irish and Lilycrop, 1999) however terrain, amount of vegetation cover, and weather conditions affect the quality of the results (Hodgson and Bresnar, 2004). One-meter per pixel LiDAR data of Amboy and Obsidian Dome was obtained from OpenTopography (www.opentopography.org) and through personal communication with Dr. Steven Anderson and Adam LeWinter to determine roughness features greater than a meter.

2.3.3 High Resolution Digital Elevation Models

The Mars Reconnaissance Orbiter (MRO) launched in 2005 with the goal of finding evidence persistent water on the surface of Mars (McEwen et al., 2007). The orbiter carries six research tools including the HiRISE and CTX cameras (Malin et al., 2007). The HiRISE products have a pixel resolution as low as 0.25 meters per pixel in visible light wavelengths, and 1 meter in near-infrared wavelengths (Kirk et al., 2008). To obtain high resolution topographic data of Mars, stereo pairs of HiRISE images showing the same area from different observation angles are processed into DEMs (Li et al., 2011; Kirk et al., 2008). Images are corrected to remove distortion then triangulated to the Mars Orbiter Laser Altimeter (MOLA) global elevation map (Li et al., 2011). The terrain model is produced by a sophisticated software pipeline and any remaining inaccuracies are removed. Resolution slightly decreases during DEM creation, resulting in topographic products that are 1 – 2 meters per pixel (Kirk et al., 2008). Producing a HiRISE DEM is a labor and time-intensive process, so readily available visible light datasets greatly outnumber topographic data (Li et al., 2011). Though high resolution topographic coverage of the planet is steadily increasing, imaging areas for HiRISE are chosen based on scientific importance to upcoming missions and features of interest identified by Mars Global Surveyor, Mars Odyssey, or CTX images (Malin et al., 2007).

CHAPTER III

METHODOLOGY

The goals of this project are to develop a cost-effective, repeatable method to compare lava surface roughness of multiple volcanic environments at a variety of scales and investigate the effect of mantling on roughness. First, I acquired high resolution topography for the analogue sites using SfM (Agisoft, 2018; Verma and Bourke, 2018) and LiDAR, as well as topography data of Tharsis from HiRISE DEMs. Then I apply two new approaches to determining roughness on lava flows – the Topographic Position Index (TPI) and Roughness Doughnut (RD). Finally, I compare the terrestrial roughness values and patterns to those on Mars and use Principal Component Analysis (PCA) to better understand the relationships between terrestrial and martian roughness.

Topographic Position Index (TPI) and Roughness Doughnut (RD) surface roughness values of Martian lavas were then compared to roughness of Hawaiian and Californian lavas from sub-meter to decameter scales. TPI is an extension for ArcGIS 10 that calculates roughness values across a DEM and creates groupings of similar roughness values within the study area. The TPI extension uses detrended (corrected to decrease the effect of local slope) elevation grid data to automatically categorize each cell based on the elevation and slope of neighboring cells. RD is similar to the TPI, however elevation data is not adjusted for regional slope, and an annular neighborhood geometry was used in place of a circular one.

3.1 Field Data Collection

3.1.1 Mauna Ulu, Hawaii

On March 30 and 31st, 2018, I established a survey area on pahoehoe flows from the 1969-1974 eruption of Mauna Ulu, Hawaii. This was a 50-meter by 50-meter area near the Chain of Craters Road in the Volcanoes National Park (Figures 1, 8). This location was selected for the variety lava flow features of different scales present within an accessible, manageable area with minimal vegetation (Figure 9). For this project I used a Nikon D3300 digital single-lens reflex (DSLR) camera with an 18-55mm variable zoom lens. The focal length was kept fixed at 24 mm while capturing the surface of this site. Following the method suggested by the Agisoft user manual (Agisoft, 2018), I photographed the surface of this flow meticulously in parallel strips while maintaining the minimum 60% overlap between all frames needed to create a gapless DEM of the site. The full site was divided into 25 10-meter by 10-meter sub sections to better track progress over both days, ensure proper coverage and improve efficiency. The 3D models of the Mauna Ulu site compile over 3000 photos.

Figure 8: Satellite Image from Google Earth showing the 50m by 50m study site on the Mauna Ulu flows, and proximity to Chain of Craters Road.

Figure 9: View from Mauna Ulu field site facing the Pacific Ocean to the south.

3.1.2 Amboy, California

At Amboy, I was unable to fit all features of interest within a single 50-meter by 50-meter area. Lava flow features were spread over greater distances than the Mauna Ulu site. For this reason, I chose to employ SfM on multiple smaller sites to ensure a variety of topographic features, scales and sand quantities were represented in DEMs. Since the primary flow features such as tumuli, folds, and inflation plateaus at Amboy were smaller than those observed at Mauna Ulu and altered by wind and sand erosion, I acquired images from four smaller sites on and off the wind streak (Figure 3). These smaller, 'focus', sites were either adjacent to or just outside of the larger study areas, and were selected to generate cm-scale DEMs of mantled areas in Agisoft PhotoScan.

Each focus site at Amboy displayed distinct textures that were too small to be clearly resolved at the DSLR focal length used at both the main Amboy sites, and in Hawaii (24 mm). These focus sites were covered in higher detail (~75% overlap) and 35mm focal length after zooming in on the surfaces. DEMs of these higher coverage,

greater zoom, and smaller areas will provide topographic data of fine-scale features without overwhelming the software. Approximately 2000 photos were used to create DEMs of four sites at Amboy.

3.2 Assessing Roughness

DEMs from SfM and LiDAR were processed in ArcGIS at a range of resolutions to determine which scale was the most effective for identifying and describing different volcanic features based on roughness, as well as the effect of mantling. This was done to confirm the resolution necessary to classify similar features and processes on Mars (Whelley et al., 2014). Traditionally, statistical analyses are used to measure changes in roughness at varying scales (Farr, 1992). I used the highest accuracy settings for image alignment, and the default settings to optimize the alignment. To obtain an accurately scaled DEM from a textured model, I chose to manually rotate and check the scale of each model.

This project utilized the Topographic Position Index (TPI) by Jenness (2006), in addition to the Roughness Doughnut method adapted for this project. Typically, most roughness investigations describe surfaces using the root-mean-square (RMS) height of a topographic profile (Bretar et al., 2013; Farr, 1992; Smith, 2014; Tian et al., 2011). RMS is a measure of how much the surface deviates from a perfectly smooth plane equal the mean of all elevation values across the profile. Elevations are squared to remove negative values, then these squared values averaged. Finally, the square root is calculated. This is also referred to as the standard deviation of elevation. RMS is very useful as a tool for vertical roughness, but it does not incorporate horizontal patterns (Bretar et al., 2013). To accurately reflect lava surface roughness, elevations in 360 degrees around a point should

be considered, rather than only measuring topographic changes along one horizontal direction. For this reason, we opted to use circular and annular cell neighborhoods to describe roughness values at each site. Furthermore, doughnut-shaped cell neighborhoods show if the average elevation within the annulus is higher or lower than the central cell which has the potential to show low areas preferentially infilling with aeolian material, an ability that the other roughness approaches lack.

3.2.1 The Topographic Position Index

As shown in Figure 10, a positive TPI indicates that the cell is higher in elevation (or more steeply sloping) than the average of its neighbors up to a specified distance away, whereas a negative one shows the cell is lower than the average surrounding elevations (Figure 10) (Equation 1) (Weiss, 2001; Jenness, 2006). The cell is classified by the magnitude of the difference in elevation along with the slope value. The cell neighborhood can be adjusted to produce varying TPI values for different scales, thus changing the scale of roughness being measured (Jenness, 2006). This extension was originally created for use in geomorphology- and hydrology-based projects (Brasington et al, 2012; Jenness, 2006) but may be useful in assessing the topographic characteristics of a lava flow surface by building a catalogue of features present at each scale. This project utilized circular TPI neighborhoods at sub-meter, 1-, 10-, 25-, and 50-meter scales. However, since the TPI method averages all values within a specified radius, the roughness patterns and values were not distinct especially at small scales (<10m).

$$TPI = \frac{central\ cell - mean\ of\ elevations\ in\ the\ circle}{Standard\ Deviation\ of\ elevations\ in\ the\ circle} \quad (1)$$

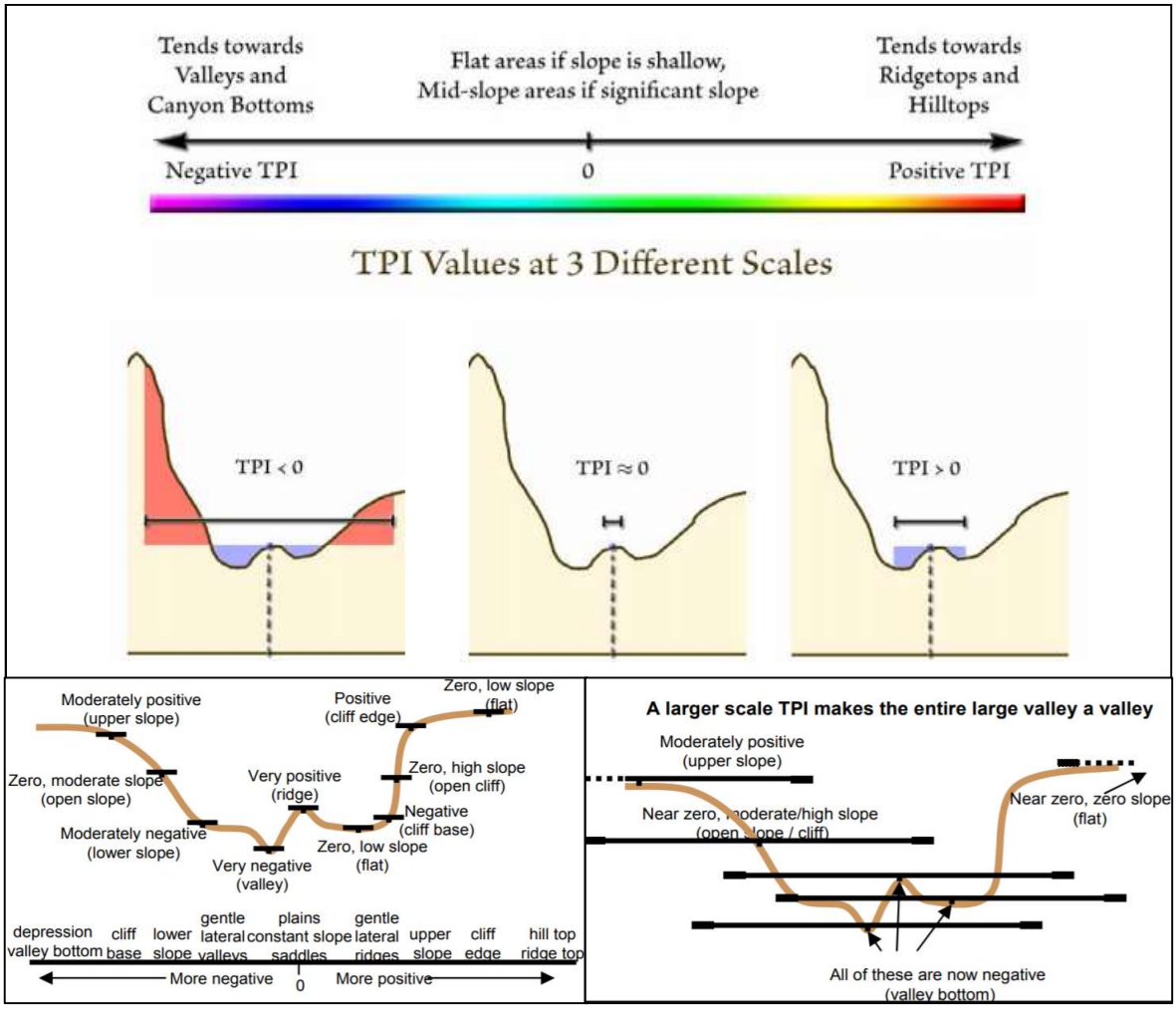

Figure 10a (above): Image showing the effect of neighborhood scale on TPI elevation. (Jenness, 2006).
Figure 10b (below): Image showing the effect of neighborhood scale on TPI slope position (Weiss 2001).

3.2.2 The Roughness Doughnut Method

The Roughness Doughnut (RD) method is a modified TPI approach that uses the Focal Statistics and Raster Calculator features in ArcGIS to produce a raster that effectively visualizes roughness at a specified scale. The goal of the RD was to compare only the elevations a certain distance away from the main cell but in every direction, rather than comparing and averaging all cells within a specified radius around the main pixel. To achieve this, I modified the TPI method so that only elevations a certain

distance from the central cell are considered. This provides a scale-dependent measure of roughness while also preserving data on the relative position of the source cell compared to average, which may be useful in determining if an area is mantled by aeolian material. Focal statistics generates a new raster based on a statistic of all the cells in the selected neighborhood of the original DEM. The statistics used for this project were mean and range. The neighborhoods were annular, or doughnut-shaped, with one circle inside of another. Only cells that were located outside the radius of the smaller circle but within the larger circle were counted as part of the neighborhood. As with TPI, the size of the neighborhood was adjusted to change the scale of roughness features being observed. In this case, the inner radius, or 'doughnut hole', was changed while the outer radius or 'doughnut thickness' stayed constant at 2-3 cells larger than the inner circle to ensure only elevations near the inner circle radius were considered. Inner radii were 1-,10-, 50-, and 100-meters. Cells that had no elevation data attached, most often due to DEM dataset artifacts or errors, were excluded from calculations. After creating new rasters for the mean and range of elevation values for a specific scale, Raster Calculator was used to find the RD value by Equation 2:

$$\frac{mean\ of\ points\ in\ the\ annulus - central\ point}{range\ of\ points\ in\ the\ annulus} = RD \qquad (2)$$

Based on this equation, a larger value indicates a minimal amount of topographic change of points in the annulus at the selected scale (the range), since the difference between the actual point and the average is larger than the range of values. A small value represents the inverse of this – the range is larger than the mean and central values, so there is a wider variety of elevations present. Values approaching 0 represents a smooth surface at the scale of the RD radius – there is no difference in the mean of values or in

the annulus, compared to the central point. Unlike standard deviation, RD values can be positive or negative. Values below 0 indicate more topographic variation in surrounding cells than the central cell.

Though the TPI and RD methods have similarities, there are a few key differences. First, only TPI detrends the data during processing. Therefore, regional slope may influence the roughness values calculated by RD. Additionally, the TPI method includes all values within the circular neighborhood to find the averages of slope and elevation that it uses to calculate the final value. This produces a more general roughness signature compared to RD which only includes cells within a tight 1-2 cell annulus along the circumference of the 1-, 10-, 50- and 100-meter specified radii.

Basaltic lava flows flow farther before cooling than lavas with higher silica content due in part to their lower viscosity. As a result, the flows are typically much thinner than their silicic counterparts. At a location dominated by overlapping basalt flows, we expect the range of values to remain low at all scales since, except for tumuli and inflation features, pahoehoe does not typically have dramatic variations in height over decameter and larger scales. Silicic environments, such as the Mono-Inyo Domes in California, form from more viscous lavas and are anticipated to be rougher at each scale (Lopes and Kilburn, 1990; Anderson et al., 1998; Stofan et al., 2000; Plaut et al., 2002).

3.3 Comparisons to Roughness on Mars

I then compared roughness values from Amboy and Mauna Ulu to lava flows on Mars. To directly describe roughness of larger martian features, I obtained DTMs of lava flows from the University of Arizona HiRISE online database. I described lava flow roughness using both the TPI and RD methods. Hawaii's pristine flows provide us with

roughness values of fresh lava surfaces, Amboy features recent lava surfaces partially covered by sand, and Martian flows could span what is observed at both sites. Thus, data from both locations on Earth should provide the range of roughness measurements needed for a full comparison of terrestrial lava flows with flows on Mars.

3.4 Principal Component Analysis

Principal Component Analysis (PCA) is statistical method of data compression. It is used to reduce a large dataset of correlated variables without sacrificing important information contained within the data. This method transforms the related variables into a smaller group of unrelated variables known as principal components. The first principal component contains most of the variability in the dataset, and successive components gradually account for less variability. The mean, variance, skewness and kurtosis of the distributions of RD, TPI and slope were calculated in Excel. The PCA was completed using the *remotes* (Csárdi et al., 2018) and *ggbiplot* (Vu, 2011) packages in R version 3.5.1 (R Core Team, 2015). PCA is often applied to geologic research with broad, complex datasets. For example, Bywater-Reyes et al. (2017) used PCA to identify the physiographic variables best related to sediment yield, whereas Burzynski (2015) utilized PCA and machine learning to classify lava lake thermal patterns and relate them to eruption processes. PCA was used highlight trends in roughness variables at different scales and locations.

CHAPTER IV

RESULTS

This chapter presents lava surface roughness values obtained from TPI and RD methods applied to the Mauna Ulu, Amboy, Obsidian Dome and Tharsis sites at a variety of scales. DEMs generated using SfM are shown first, followed by TPI maps and RD maps of each field location. Although Obsidian Dome was not a key part of this project, 1 meter per pixel LiDAR data was obtained from the Opentopography website (opentopo.sdsc.edu) to illustrate the roughness differences between silicic and mafic lava flows. TPI values are higher along the surface of Obsidian Dome than TPI values at the other locations, at every scale observed, consistent with observations by Plaut et al. (2004). Only the best, most complete Agisoft model from each site was selected to create a DEM with sub-meter resolution that would be representative of large-scale processes at that location. At Mauna Ulu, the best model was of section #22 (Figure 11), whereas focus site #4 was the best product from Amboy (Figure 12).

4.1 Digital Elevation Models Using Structure from Motion

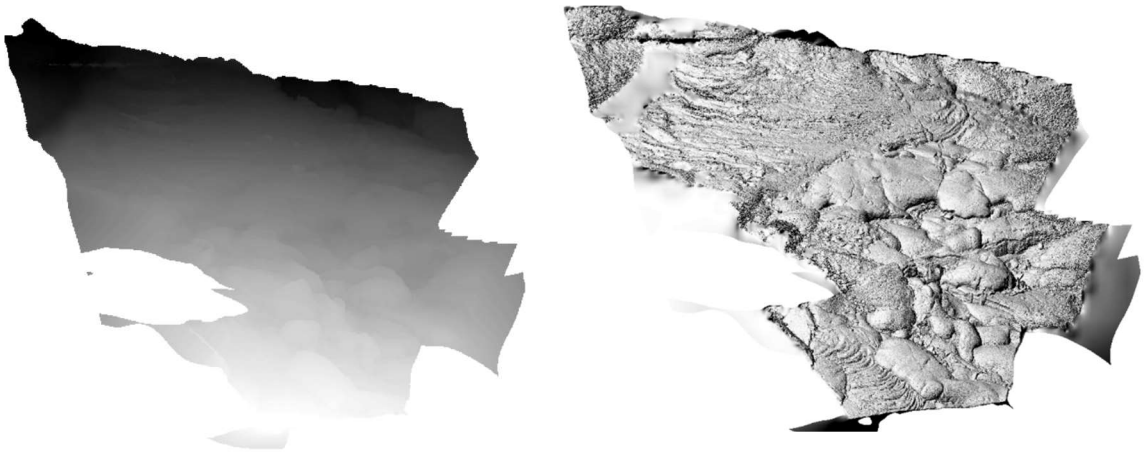

Figure 11a (left): DEM of Mauna Ulu SfM section #22. Figure 11b (right): Hillshade of this DEM.

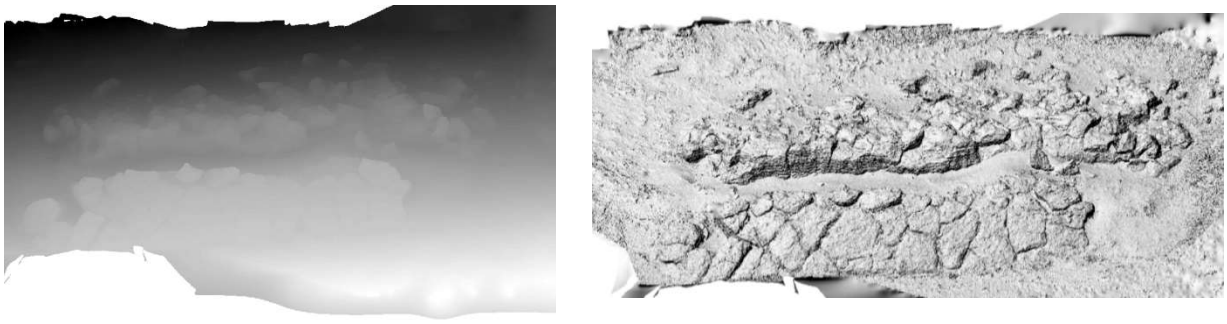

Figure 12a (left): Digital Elevation Model of focus site #4 at Amboy. Figure 12b (right) A view of this DEM with hillshade applied in ArcGIS.

4.2 Topographic Position Index

4.2.1 Obsidian Dome

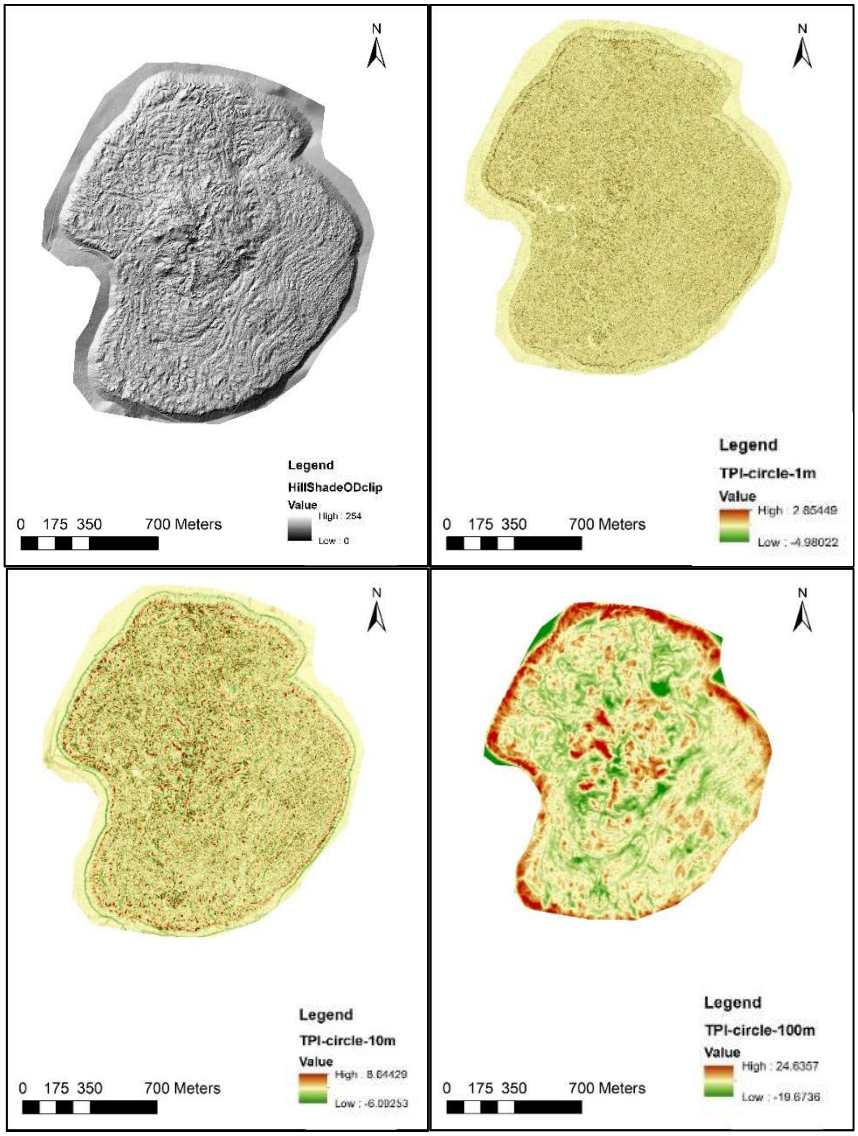

Figure 13a (top left): Hillshade of Obsidian Dome.
Figure 13b (top right): TPI map of Obsidian Dome, California at the 1-meter scale.
Figure 13c (bottom left): TPI map of Obsidian Dome, California at the 10-meter scale.
Figure 13d (bottom right): TPI map of Obsidian Dome, California at the 100-meter scale.

4.2.2 Mauna Ulu Section #22

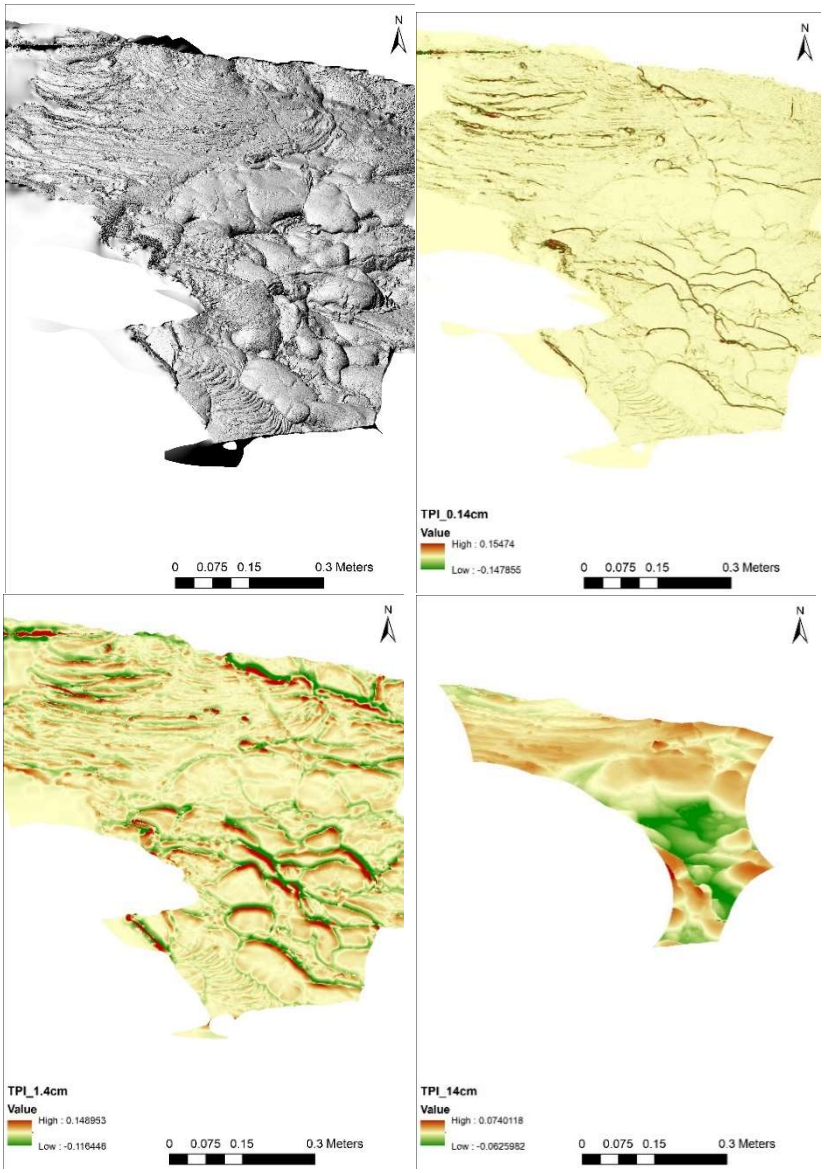

Figure 14a (top left): Hillshade of Mauna Ulu section #22
Figure 14b (top right): TPI map of Mauna Ulu section #22 at the 0.14cm scale.
Figure 14c (bottom left): TPI map Mauna Ulu section #22 at the 1.4cm scale.
Figure 14d (bottom right): TPI map of Mauna Ulu section #22 at the 14cm scale.

At Mauna Ulu, TPI values from 0.143 centimeter per pixel SfM DEMs had a range of -0.14 to 0.15. Ropey folds show an alternating pattern of low-high-low values in a wave-like pattern. Overlapping pahoehoe toes display a scalloped pattern of roughness characterized by high TPI values immediately followed by low ones (Figure 14). The

scale of features highlighted here appear to be flow margins, rippling folds and cracks less than a meter in size. Intermediate TPI values were assigned to the flat spaces surrounding more distinct features. The lowest values aligned with ripples, and cracks.

4.2.3 Amboy Focus Site #4

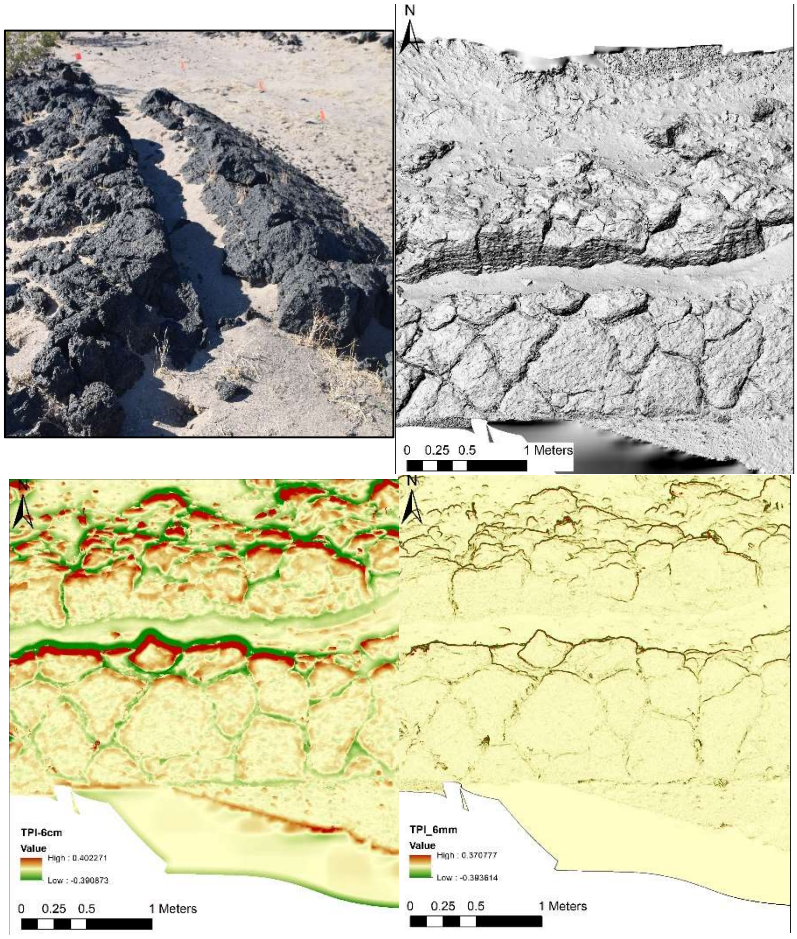

Figure 15a (top left): Visible light image of Amboy Focus site #4
Figure 15b (top right): Hillshade of Amboy Focus site #4.
Figure 15c (bottom left): TPI values for Amboy Focus site #4 at the 6mm scale.
Figure 15d (bottom right): TPI values for Amboy Focus site #4 at the 6cm scale.

The DEM from SfM focus site #4 had TPI ranges from -0.4 to 0.4. The roughest areas, marked by the highest TPI values (>0.2), outlined the top and sides of large cracks in the lava. Intermediate TPI values (-0.2< x <0.2) were assigned to the polygonal

fractured plates and sand filling in the base of the large crack bisecting the site. The lowest values (<-0.2) were clustered in the base of smaller cracks on the surface of the feature.

4.2.4 Amboy Light Detection and Ranging

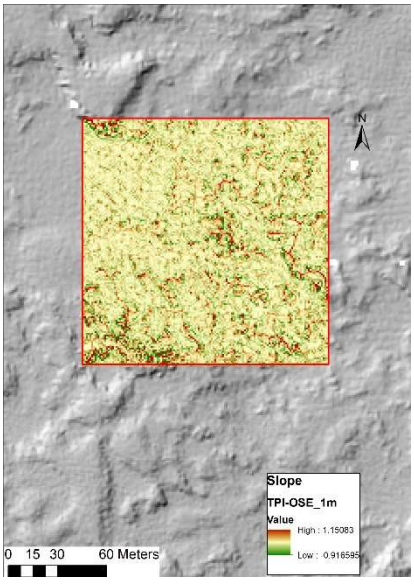

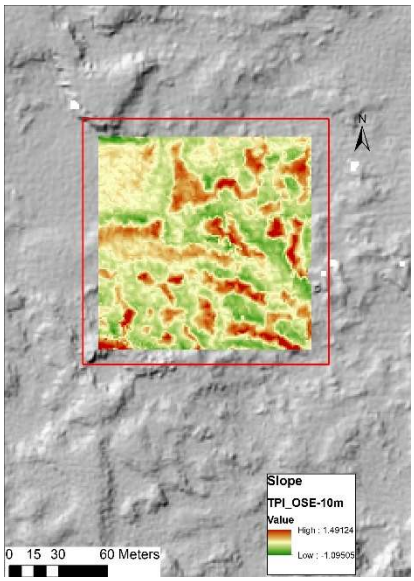

Figure 16a (left): TPI values at the 1-meter scale on an area outside of the wind streak at Amboy.
Figure 16b (right): TPI values at the 10-meter scale on an area outside of the wind streak at Amboy.

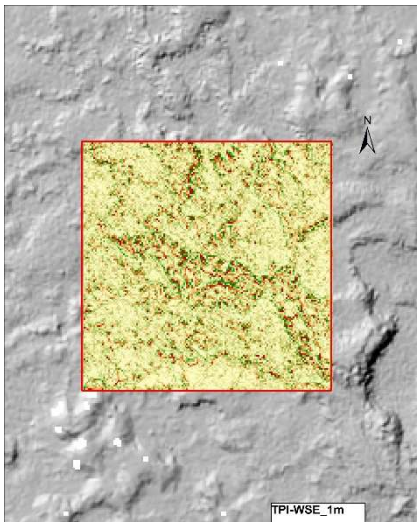

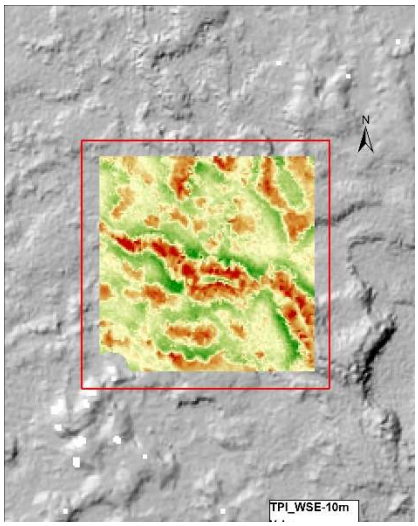

Figure 17a (left): TPI values at the 1-meter scale on an area within the wind streak at Amboy.
Figure 17b (right): TPI values at the 10-meter scale on an area within the wind streak at Amboy.

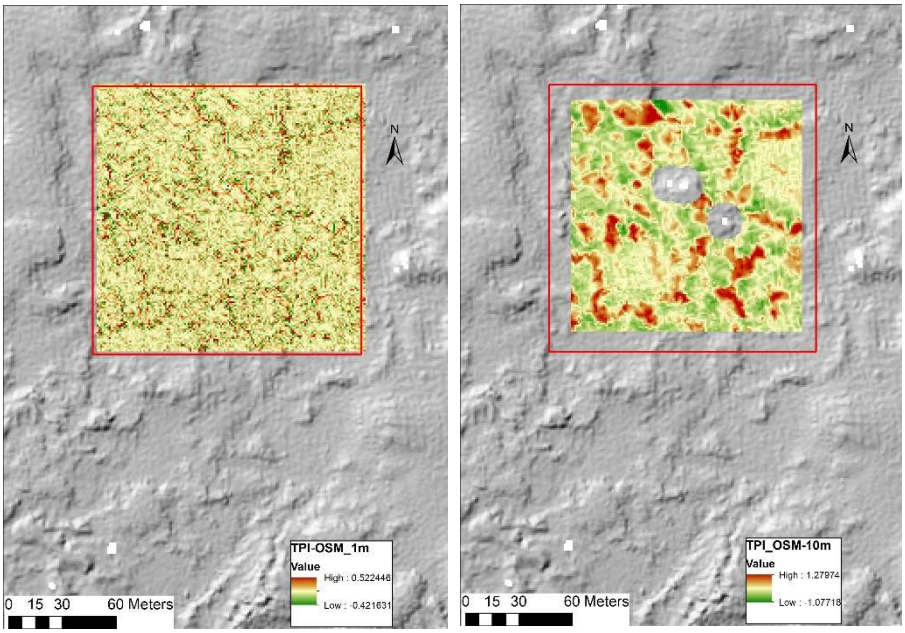

Figure 18a (left): TPI values at the 1-meter scale on an area within the wind streak at Amboy.
Figure 18b (right): TPI values at the 10-meter scale on an area within the wind streak at Amboy.

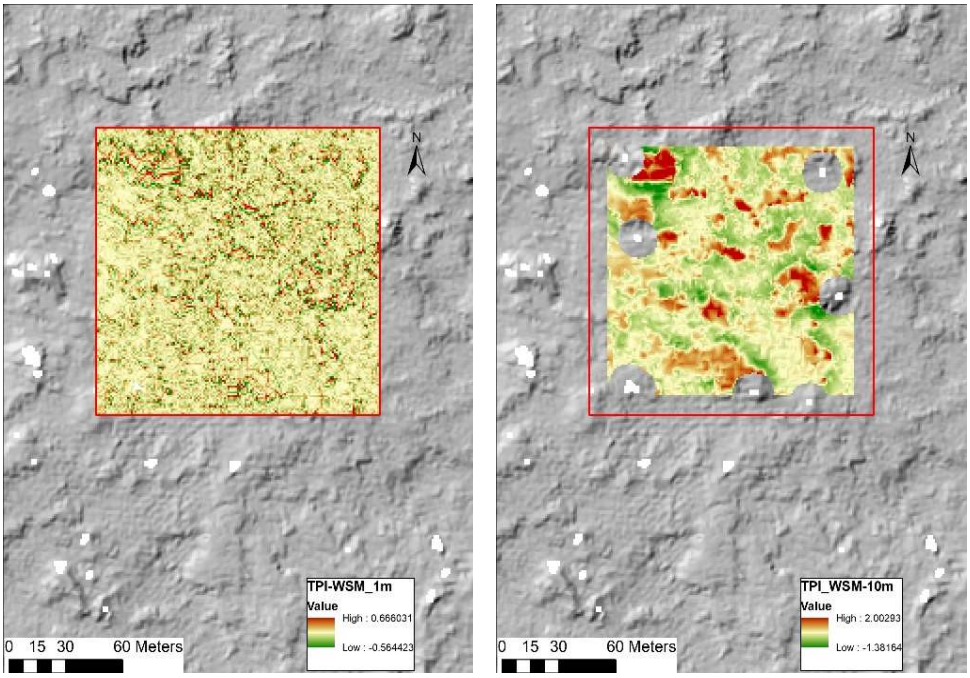

Figure 19a (left): TPI values at the 1-meter scale on an area within the wind streak at Amboy.
Figure 19b (right): TPI values at the 10-meter scale on an area within the wind streak at Amboy.

TPI values at Amboy ranged from -0.9 to 2.31 on the 1 meter per pixel airborne LiDAR dataset. The sharpest transitions from low to high values were along lobate features, producing arcuate patterns (Figures 16-19). The scale of features highlighted here appear to be flow margins and flow toes upwards of 5 meters in size. The one-meter TPI maps were not as clear as the larger scales but seem to emphasize sand deposits surrounding and covering the lava flows.

4.2.5 Tharsis

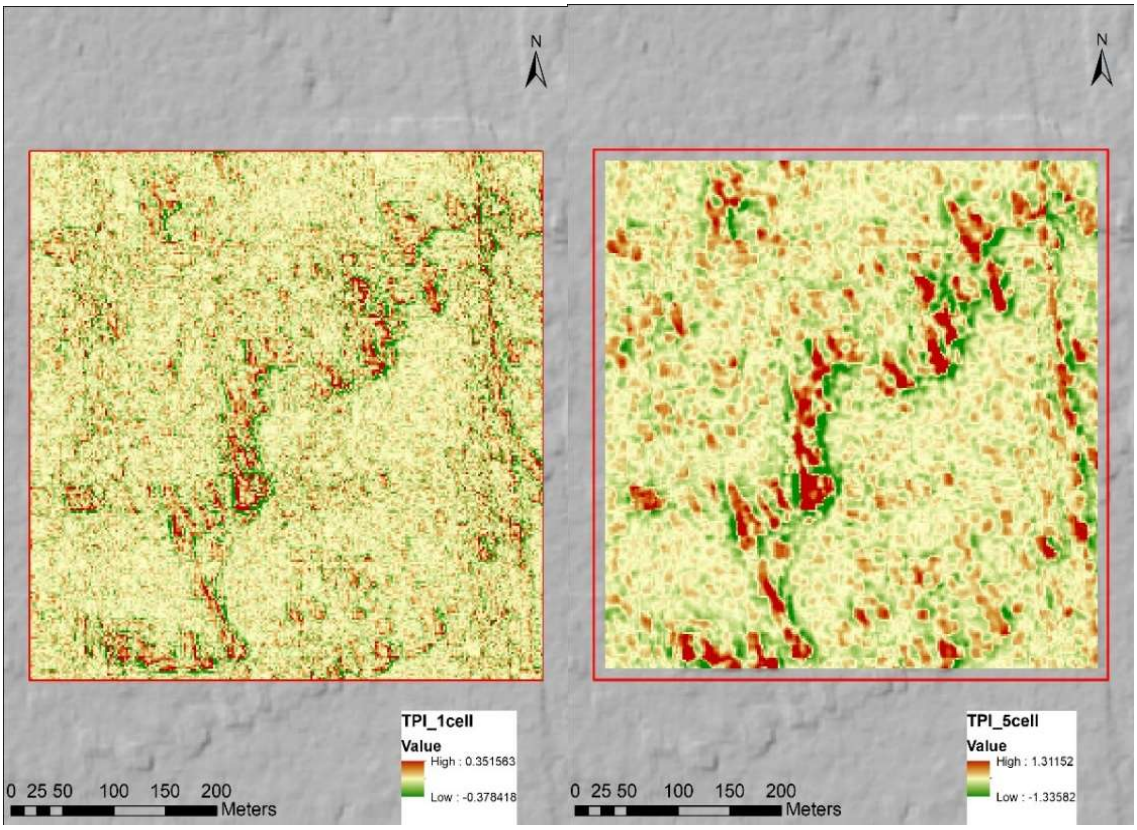

Figure 20a (left): TPI Surface roughness at the 1-meter scale in the Tharsis region of Mars. Figure 20b (right): TPI roughness at the 10-meter scale in the Tharsis region of Mars.

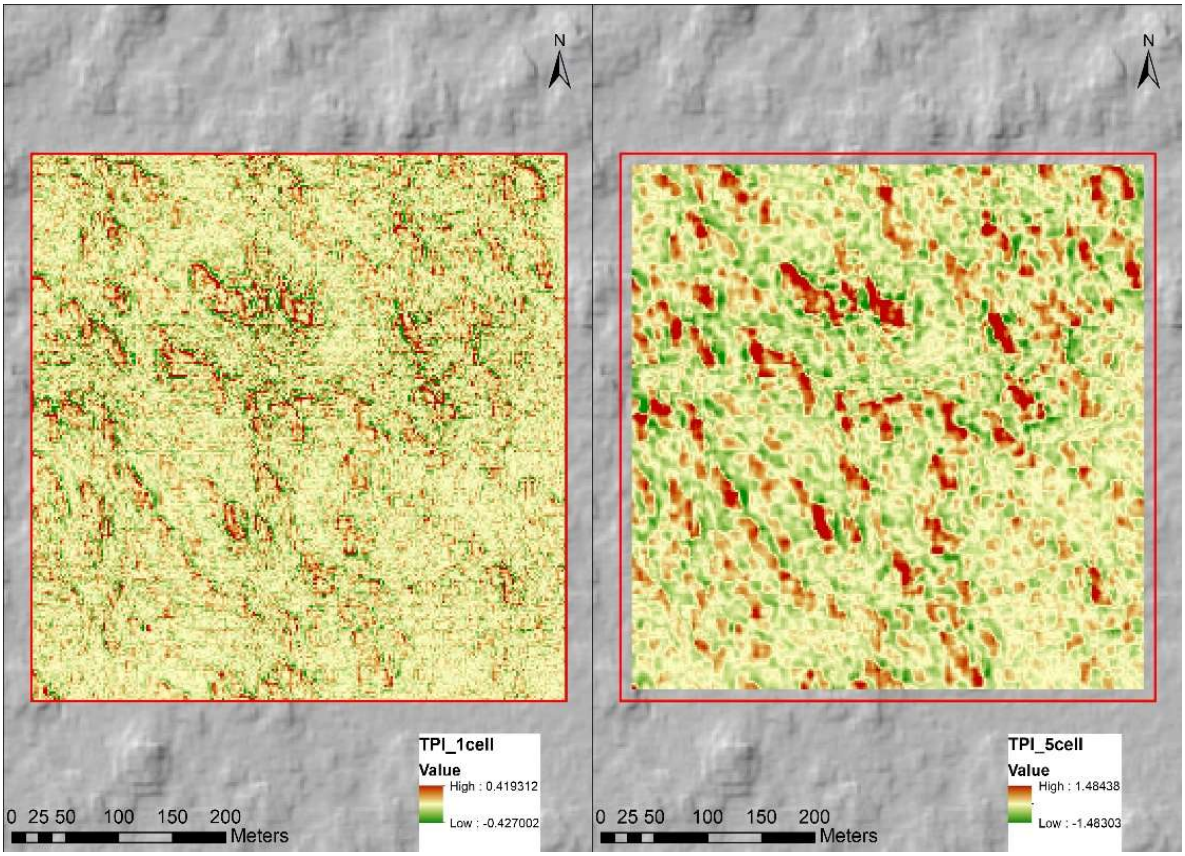

Figure 21a (left): TPI surface roughness at the 1-meter scale in the Tharsis region of Mars.
Figure 21b (right): TPI surface roughness at the 10-meter scale in the Tharsis region of Mars.

TPI values of clipped regions near the Tharsis Tholus shield volcano span -0.4 to 0.4. This aligns with TPI values of the Amboy focus site recreated using photogrammetry. TPI maps illustrate similar patterns to those observed at the Amboy lava field in the 1 meter per pixel LiDAR dataset. Linear trends of lobate features are clearly visible at scales equal to and greater than 10 meters. Scalloped TPI patterns also outline the remnants of martian lava flows as they do at Amboy. Again, one-meter TPI maps of Tharsis are pixelated but show undulating patterns on the surface of the flows related to sand dunes. TPI values for the Amboy and Mauna Ulu SfM DEMs decrease as

neighborhood radius increases whereas the TPI roughness values for the Amboy LiDAR and Tharsis DEMs increase along with radius.

4.3 Roughness Doughnut

As described in the Methodology section, the RD method displays roughness values relative to a focus cell, based on neighborhood elevation statistics. RD considers cells along the circumference of a circle, unlike the TPI which averages all points within the full area of the circle, thereby dampening roughness signals at a specific distance from the source cell. RD values and related elevation products should identify surfaces partially mantled by sand cover as sand should preferentially fill in low areas resulting in a lower elevation range and less positive RD values than a non-mantled surface. The larger the RD value, the lower the topographic variation at the selected scale. A small value represents the inverse of this – a wider variety of elevations at the scale.

4.3.1 Obsidian Dome

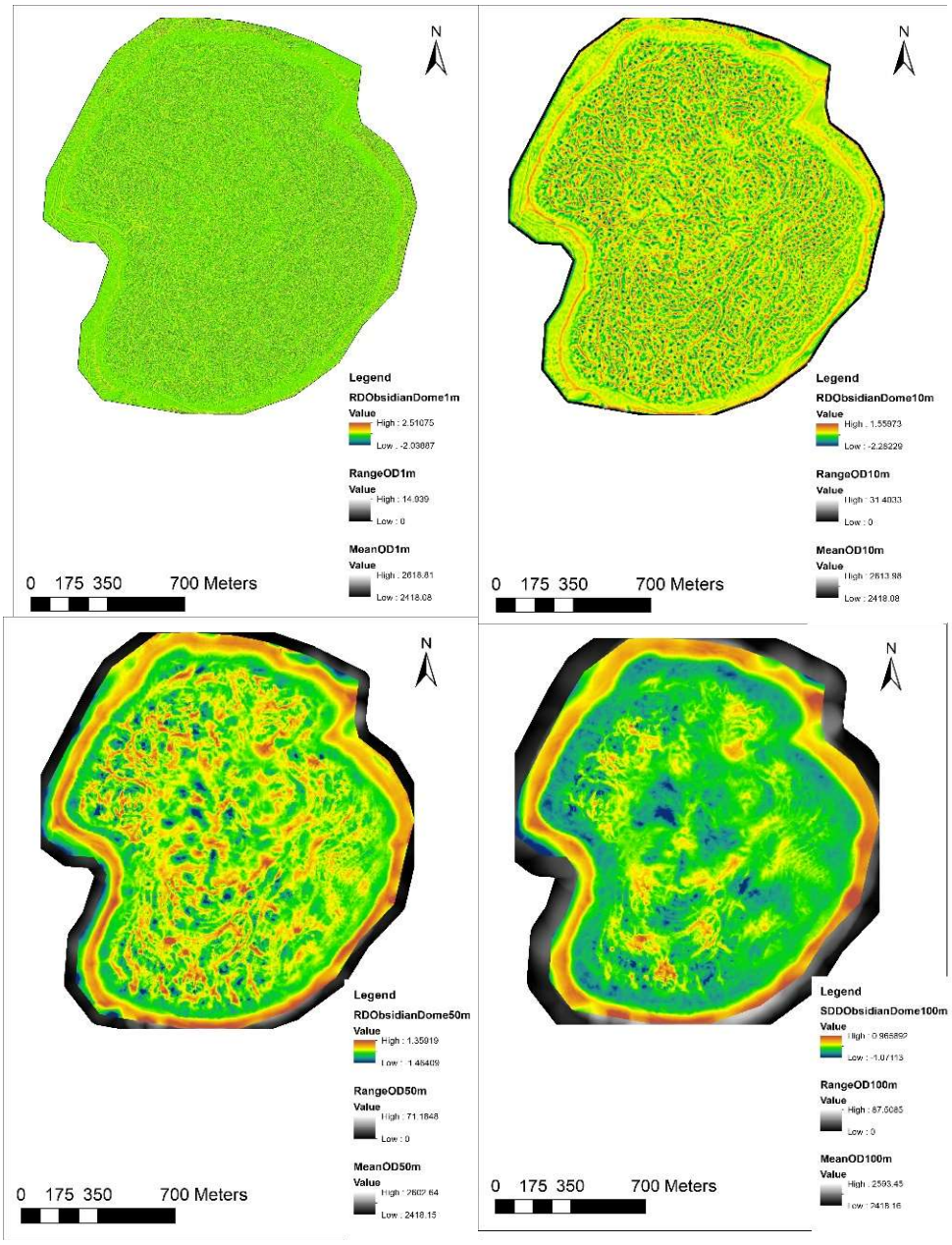

Figure 22a (top left): RD map of Obsidian Dome, California at the 1-meter scale.
Figure 22b (top right): RD map of Obsidian Dome, California at the 10-meter scale.
Figure 22c (bottom left): RD map of Obsidian Dome, California at the 50-meter scale.
Figure 22d (bottom right): RD map of Obsidian Dome, California at the 100-meter scale.

4.3.2 Mauna Ulu Section #22

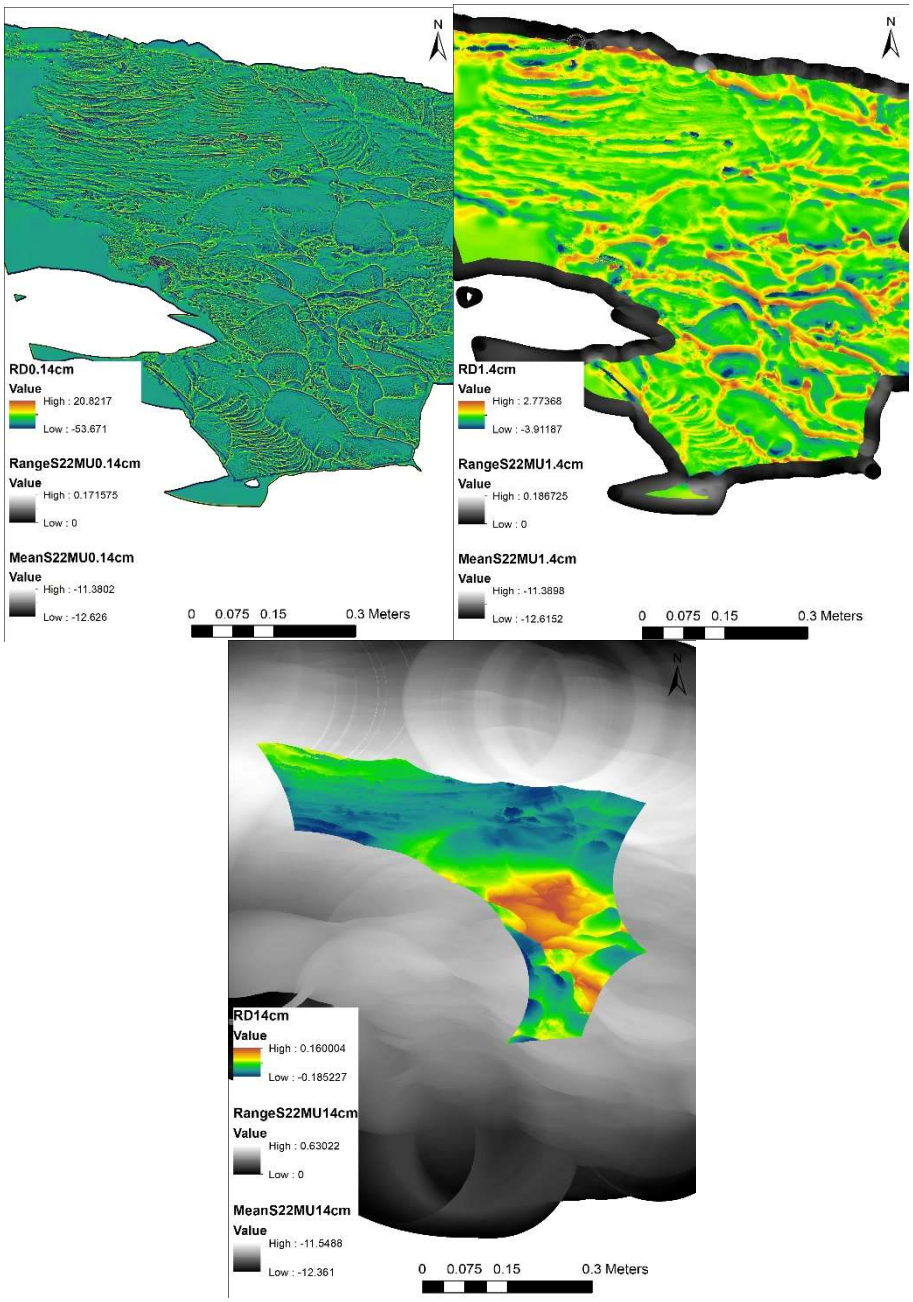

Figure 23a (top left): RD map of Mauna Ulu section #22 at the 0.14cm scale.
Figure 23b (top right): TPI map Mauna Ulu section #22 at the 1.4cm scale.
Figure 23c (bottom): TPI map of Mauna Ulu section #22 at the 14cm scale.

4.3.3 Amboy Focus Site #4

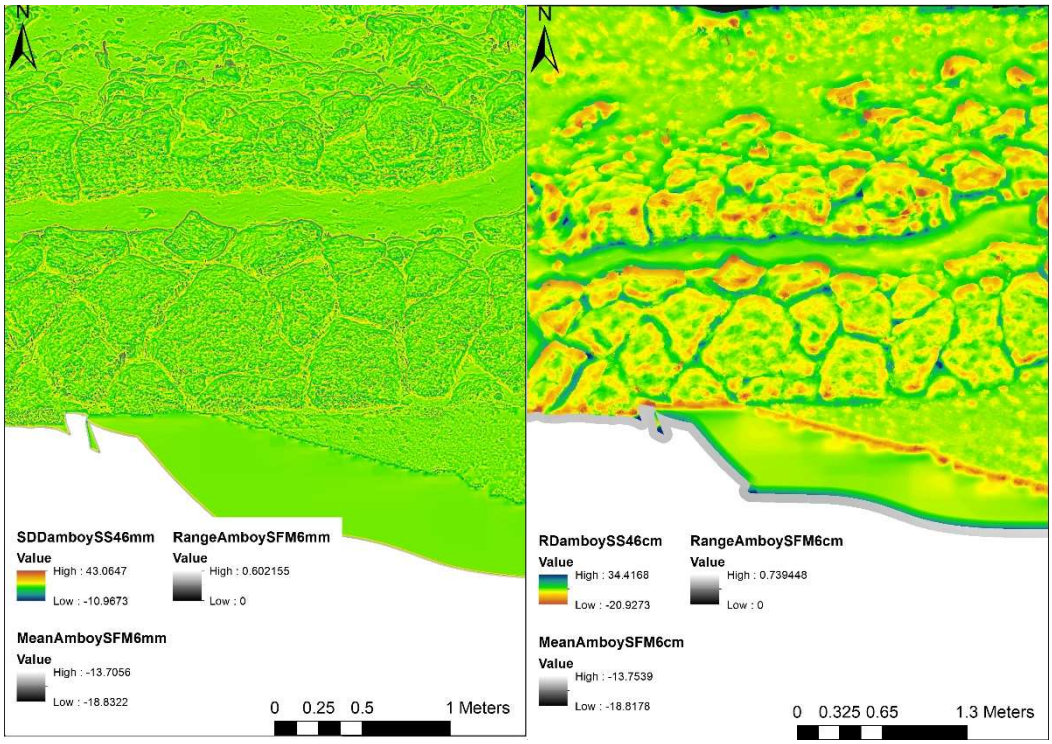

Figure 24a (left): RD values for Amboy Focus site #4 at the 0.6cm scale.
Figure 24b (right): RD values for Amboy Focus site #4 at the 6cm scale.

4.3.4 Amboy Light Detection and Ranging

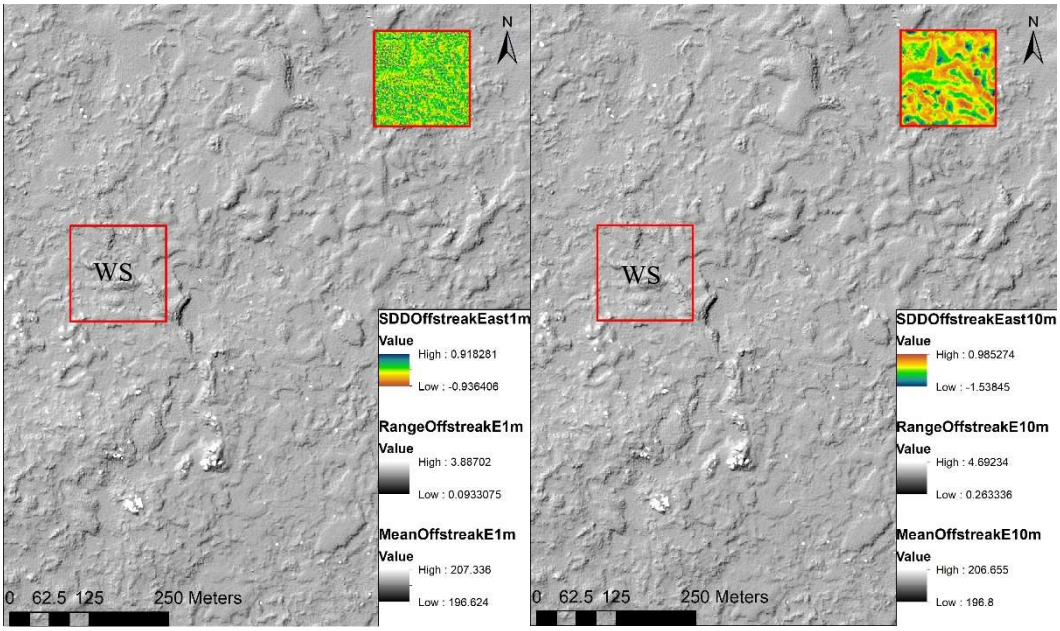

Figure 25a (left): RD values at the 1-meter scale on an area outside of the wind streak at Amboy.
Figure 25b (right): RD values at the 10-meter scale on an area outside of the wind streak at Amboy.

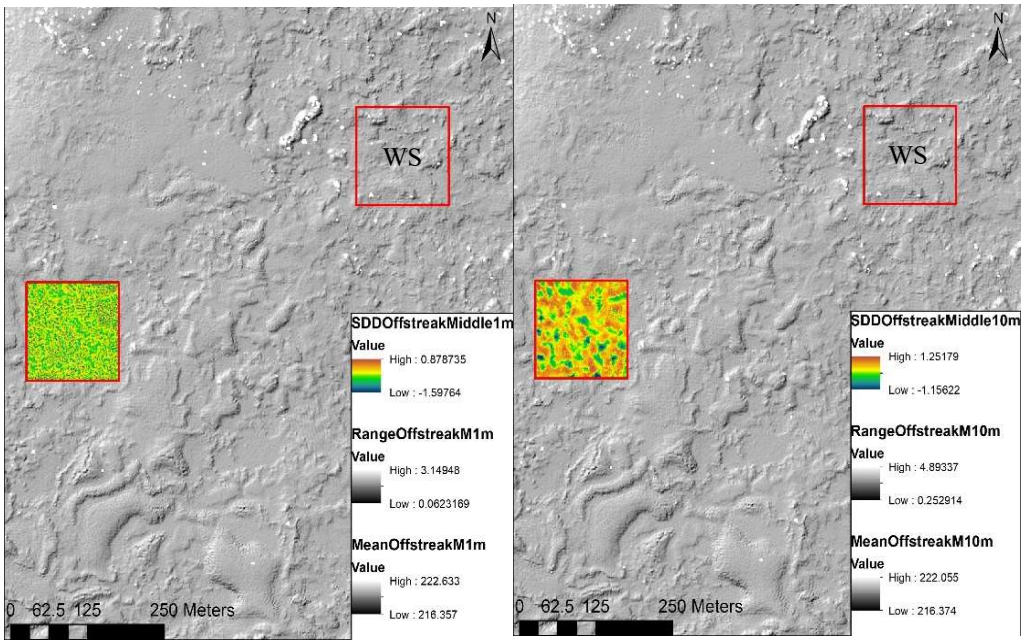

Figure 26a (left): RD values at the 1-meter scale on an area outside of the wind streak at Amboy.
Figure 26b (right): RD values at the 10-meter scale on an area outside of the wind streak at Amboy.

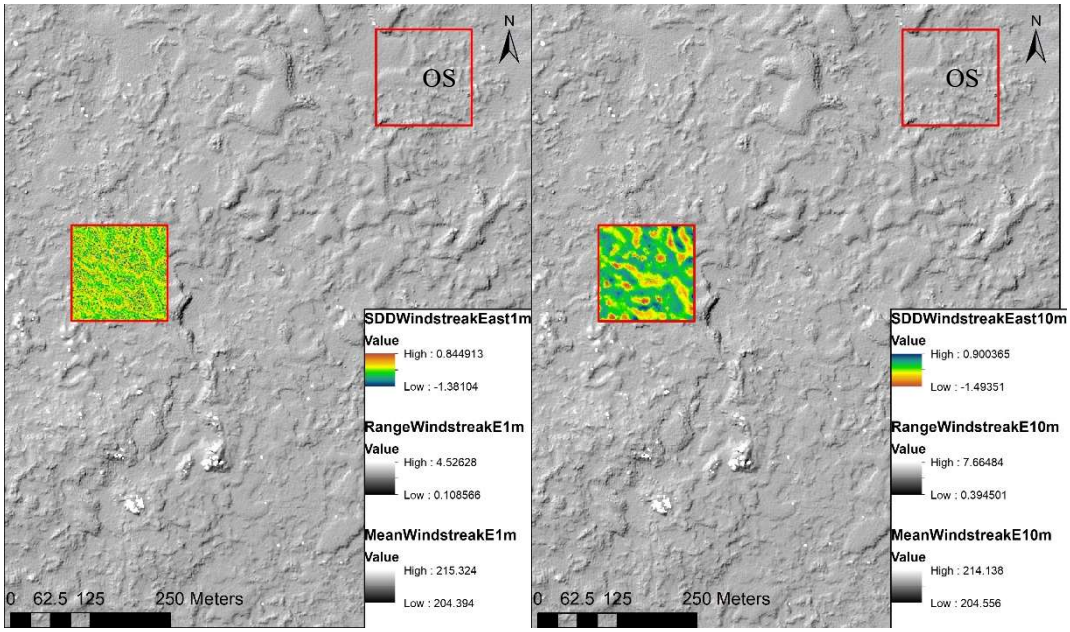

Figure 27a (left): RD values at the 1-meter scale for an area within the wind streak at Amboy.
Figure 27b (right): RD values at the 10-meter scale for an area within the wind streak at Amboy.

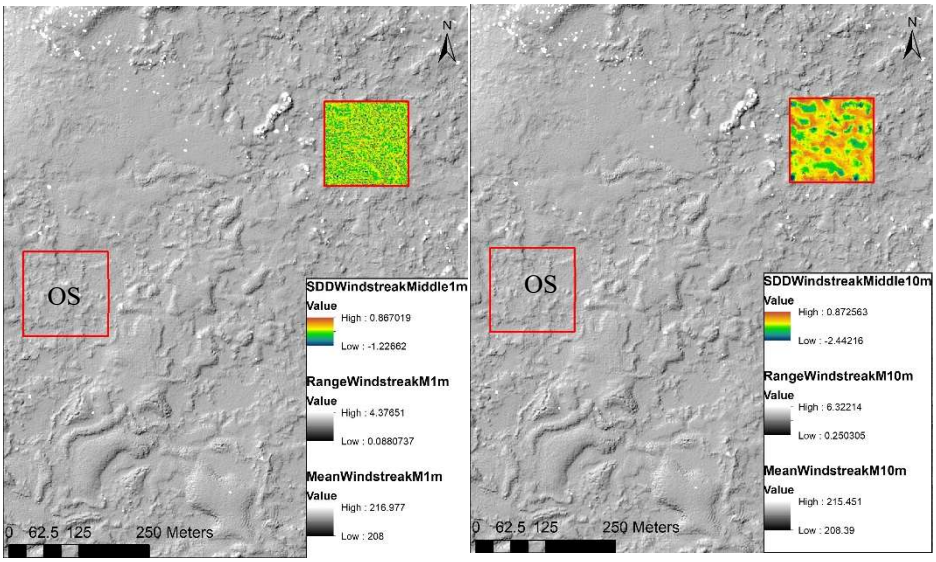

Figure 28a (left): RD values at the 1-meter scale on an area within the wind streak at Amboy.
Figure 28b (right): RD values at the 10-meter scale on an area outside of the wind streak at Amboy.

RD values acquired for the airborne LiDAR dataset at Amboy ranged from -2.44 to 1.25. Ten-meter maps show the general outline of the exposed lava but not with the detail shown by TPI.

4.3.5 Tharsis

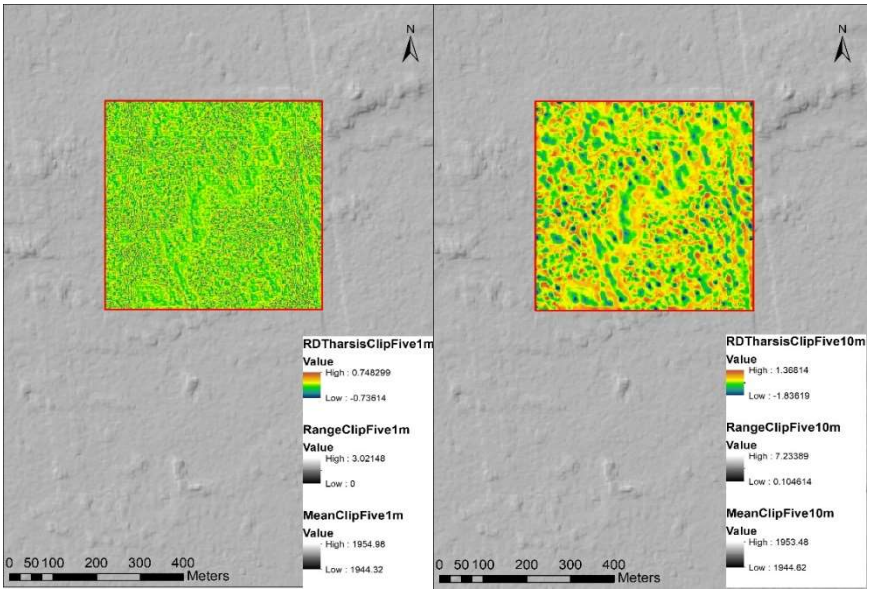

Figure 29a (left): Surface roughness at the 1-meter scale in the Tharsis region of Mars.
Figure 29b (right): Surface roughness at the 10-meter scale in the Tharsis region

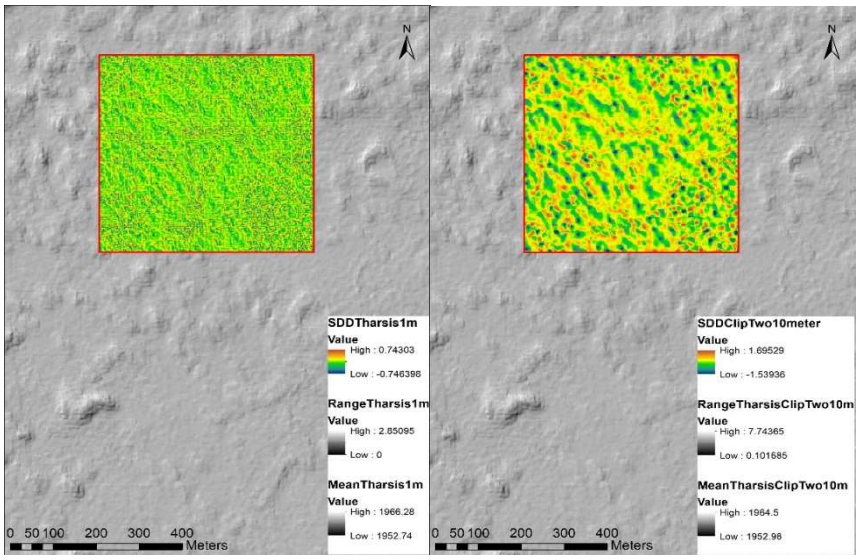

Figure 30a (left): Surface roughness at the 1-meter scale on an area in the Tharsis region.
Figure 30b (right): Surface roughness at the 10-meter scale on an area in the

At Amboy and Mauna Ulu, RD values decrease as doughnut radius increases. The opposite is true for lava flows on Tharsis – they show an increase in RD as the doughnut radius widens. Table 3 below summarizes the results of TPI and RD at each scale and location.

Table 3: Results summary

		TPI Scale				RD Scale			
Site	Resolution	1m	10m	50m	100m	1m	10m	50m	100m
Obsidian Dome	1m/ pixel LiDAR	-4.9 to 2.8	-6.0 to 8.6	-12 to 17	-19.6 to 24.6	-2.0 to 2.5	-2.28 to 1.5	-12.5 to 17.7	-19.6 to 24.6
Amboy - WS	1m/ pixel LiDAR	-0.8 to 0.9	-1.8 to 2.1			-1.2 to 0.88	-1.48 to 0.9		
Amboy - OS	1m/ pixel LiDAR	-1.5 to 0.9	-1.5 to 1.2			-1.59 to 0.91	-1.53 to 1.25		
Tharsis, Mars	2m/pixel HiRISE DEMs	-0.4 to 0.4	-1.48 to 1.48			-0.74 to 0.74	-1.8 to 1.6	-2.5 to 6.0	-3.25 to 6.68
		TPI Scale				RD Scale			
		0.14 cm	1.4 cm	14 cm		0.14 cm	1.4 cm	14 cm	
Mauna Ulu	0.14 cm/pixel SfM	-0.14 to 0.15	-0.11 to 0.14	-0.06 to 0.07		-53 to 20	-3.9 to 2.7	-0.18 to 0.16	
		TPI Scale				RD Scale			
		6 mm	6 cm			6 mm	6 cm		
Amboy	0.65mm/ pixel SfM	-0.39 to 0.37	-0.39 to 0.40			-0.20 to 34	-0.10 to 43		

4.4 Principal Component Analysis of Roughness Measurements

A Principal Component Analysis (PCA) was performed to condense the data while highlighting the underlying structure. The sub-meter resolution SfM datasets were analyzed separately from, as well as alongside, the LiDAR datasets to investigate any trends in roughness unique to fine-scale features. The graph shows that Obsidian Dome is characterized by far higher values of slope and RD than the other locations, consistent with other roughness studies of lava surfaces (Plaut et al., 2002; Plaut et al., 1994), whereas the Amboy data have a higher range of TPI roughness values. Tharsis data are the most tightly clustered of the locations and set apart by their higher minimum and mean RD values. Each location appears to be differentiated along PC1, whereas roughness scales are separated along PC2. Tharsis sites plot higher along PC2 than Amboy but have the lowest PC1 values of all locations.

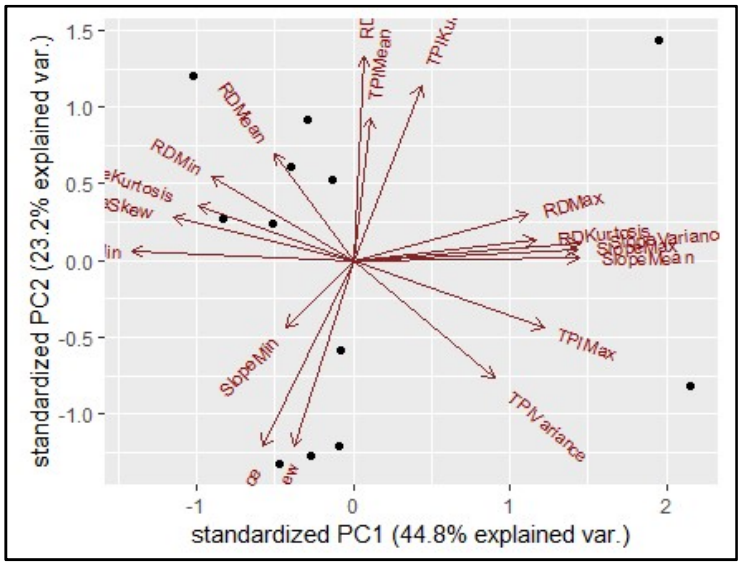

Figure 31: PCA plot showing the roughness variables most closely linked to Principal Component 1 (x-axis) and Principal Component 2 (y-axis)

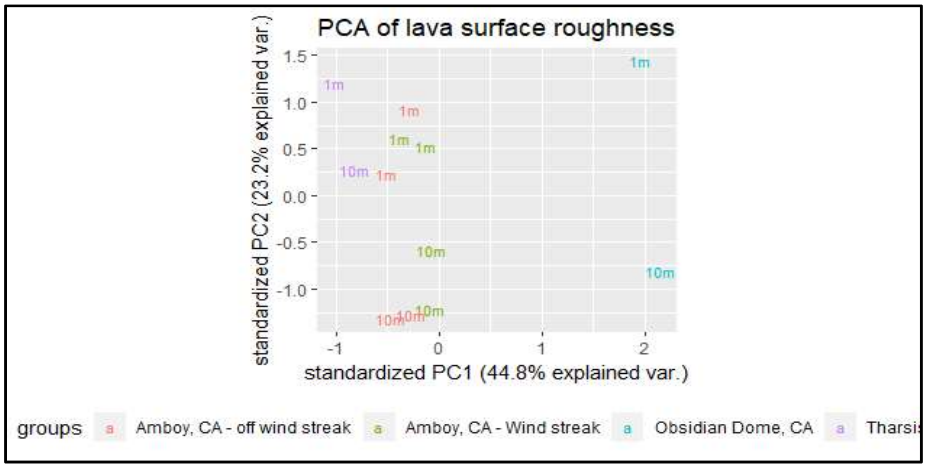

Figure 32: PCA plot showing points colour-coded by location and relabeled by scale. Variables were removed to declutter the display.

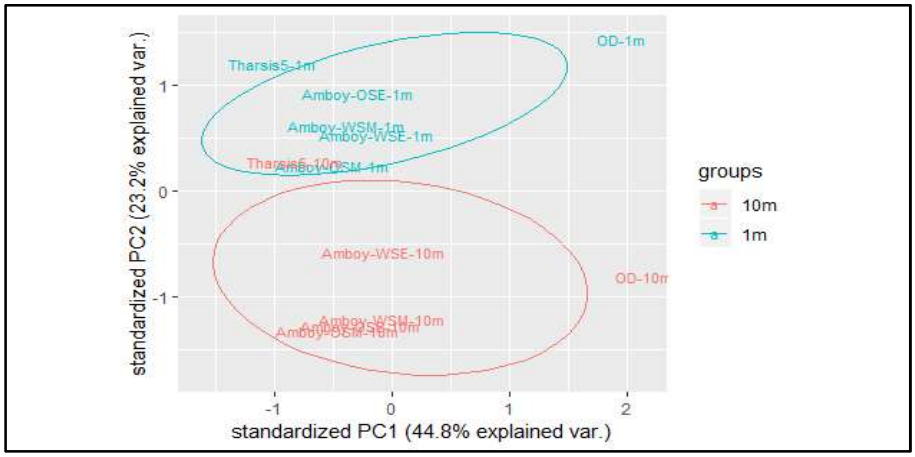

Figure 33: PCA plot showing points grouped by scale. Variables were removed to declutter the display.

CHAPTER V

DISCUSSION AND CONCLUSIONS

Roughness values from TPI and RD methods, along with their statistical moments, were assessed according to the science questions posed in the introduction. The main goals of this research project were to determine if roughness can be tied to emplacement conditions, and whether martian lava flows fit within the range of roughness observations at both analogue sites on Earth. Additional objectives were to describe the effect of mantling on roughness of lava flow features and determine if the methods presented here can positively identify mantled martian lavas. Finally, I aimed to confirm if roughness patterns produce valuable maps of terrestrial and extraterrestrial volcanic environments. These questions are addressed in the order that they were presented here.

5.1 Description of Lava Flow Features Using Roughness Patterns

My first research goal was to use roughness values and patterns to describe any visible lava flow features, and relate these features to emplacement conditions in an effort to further current understanding of martian geologic history. Table 4 summarizes the lava surface features inferred from roughness patterns at increasing scales. TPI results for the Amboy SfM focus site #4 best outlined fractures and cracks in the lava. TPI patterns based on the 1 meter per pixel airborne LiDAR dataset at Amboy displayed many volcanic features such as flow margins, lobate pahoehoe toes, and inflated platform flows.

Table 4: Lava surface features inferred from roughness values and patterns

	Small scale	Medium scale		Large scale
	Millimeter to Centimeter	Centimeter to meter	Meter	Decameter and Larger
Dataset and resolution	SfM (sub-meter)	SfM (sub meter)	LiDAR (1m)	LiDAR (1m)
TPI	-0.40 to 0.40	-0.14 to 0.15	-0.90 to 1.15	-1.84 to 2.13
RD	-20.90 to 34.41	-3.91 to 2.77	-1.59 to 0.91	-2.44 to 1.25
Inferred features	Small cracks and folds	Toe margins, ropey folds and blocks	Flow margins, aeolian deposits and bed forms	Full flow fields, sheeted flows and levees

TPI maps at the 1-meter scale were the least diagnostic, but variations from extremely high to extremely low values over short distances seem to indicate sand deposits. These sandy areas surround the edges of the lava flows which are represented by higher, consistent roughness values at the 1-meter scale (Figures 16a-19a). Lobate features displayed as arcuate TPI patterns were interpreted as flow margins greater than 5-meters high – the minimum average height of flow edges at Amboy according to Greeley and Bunch (1976). TPI radii larger than 25 meters showed channelized patterns of TPI values radiating from the Amboy Crater cinder cone and winding between some lava flow edges suggesting fluvial erosion. RD values acquired for the airborne LiDAR dataset at Amboy showed the margins of exposed lava flows at the 10-meter scale (Figures 16b-19b).

The 1-meter RD maps show sharp changes between low to moderate roughness values occurring in spaces that appear smooth on hillshade maps (Figures 25a – 28a). These are also interpreted as pockets of sand with meter to sub-meter aeolian features. Sub-meter RD values for Amboy highlight similar features as the TPI maps at the same

scales but do so more sharply (Figures 15 and 24). Additionally, though TPI and RD maps of Mauna Ulu SfM section #22 (Figures 14 and 23) show the same features, the details are better represented by RD maps. In the same way, ropey and ridged features on the surface of pahoehoe toes, as well as the scalloped pattern of overlapping toe margins, are illustrated in a more distinct way by RD.

TPI values of clipped regions near the Tharsis volcanoes are similar those of the Amboy SfM focus site. Both locations also display similar linear trends of low RD values surrounded by increasingly higher ones (Figures 29 and 30). This is attributed to sand dunes oriented by the dominant wind direction. Additionally, TPI maps of Tharsis (Figures 20 and 21) illustrate similar patterns to those observed at the Amboy lava field in the 1 meter per pixel LiDAR dataset. Linear trends of lobate features are clearly visible at scales equal to and greater than 10-meters. Separate, scalloped TPI patterns also outline the remnants of martian lava flows as they do at Amboy. Again, one-meter TPI maps are pixelated but show undulating patterns on the surface of the flows interpreted as dune forms similar to those at Amboy. Since Tharsis roughness values and patterns resemble those of Amboy more closely than Hawaii, I can infer that the lava flows in the selected martian sites share a similar emplacement and/or erosional history with Amboy. This is supported by literature describing the effusive basaltic volcanism of the Tharsis volcanic province (Greeley and Bunch, 1976; Wise et al., 1979; Finnerty et al., 1988; Watters, 1991; Mege and Masson, 1996; McEwen et al., 1999; Christensen et al., 2000; Fink and Anderson, 2000; Halliday et al., 2001; McSween et al., 2003; Finnegan et al, 2004; Bleacher et al., 2007; Lang et al., 2009; Hauber et al., 2011; Brož et al., 2017; Huges et al., 2019).

5.2 Comparison of Martian and Terrestrial Lava Flows

Recall that, whereas RD considers only cells within a 1-3 pixel wide annulus at a specified radius away, the TPI averages all points within the area of the circle resulting in slightly different roughness signals. This project compares both methods, at varying scales, for multiple volcanic environments. I calculated the mean, variance, skewness and kurtosis for both roughness methods, as well as surface slope to gain a better understanding of statistical trends at the locations. The result was a bulky dataset with many variables. I used Principal Component Analysis (PCA) to effectively visualize and draw patterns from the multivariable data. The results of the PCA showed several principal components, one for each variable put into the analysis, with PC1 accounting for 39.28% and PC2 explaining 21.06% of the total variation in the dataset. The majority of the information in the dataset (60.34%) is therefore represented by the first PCA plot (Figure 31). The graph shows that Obsidian Dome is characterized by far higher values of slope and RD than the other locations, while Amboy data have a higher range of TPI mean roughness values. Tharsis data are the most tightly clustered of the locations, and set apart by their higher minimum and mean RD values. The key takeaway therefore is that points do not overlap. When grouped by scale and location (Figures 32 and 33) it is clear that PC1 separates each location while PC2 creates a divide based on scale. PCA plots also showed that, at the 1 meter and 10 meter scales, roughness characteristics of lava flows on Tharsis are similar to lava flows surrounding Amboy crater.

5.3 Effect of Mantling on Roughness

Due to aeolian processes currently active on Mars, I was interested in observing the effect of sand mantling on lava surface roughness. I expected RD values to be higher

on more heavily mantled surfaces based on the RD raster equation. As sand settles preferentially in the lowest regions, the elevation range as well as the final RD value were expected to increase. This is true for both comparison sites at Amboy, at both the 1-meter and 10-meter scales (Figures 16-19, and 25-28). My results show that both on Earth and on Mars, mantling dampens the roughness signature of small features. Larger features such as deep pressure ridges and inflated flows are best preserved along their edges. As a result the range of elevation values increase as the observation radius widens.

Though there are similarities between martian and terrestrial lava flows, many differences also exist. A major distinction is the extent of aeolian deposition. Dust mantling at Amboy is rather light, covering up to a meter of the surface in several areas (Greeley and Bunch, 1976; Kienenberger and Greeley 2012). However, mantling on Mars is a significant global phenomenon that has been occurring for billions of years. As a result, this process has almost entirely obscured the original landforms in certain parts of the planet (Ward, 1979; Tanaka, 2000; Newsom et al., 2007; Keszthelyi et al., 2008; Hauber et al., 2011; Schon et al., 2012; Kienenberger and Greeley, 2012). Additionally, many volcanic features on Mars are orders of magnitudes larger than those on Earth (Solomon and Head, 1982; Mege and Masson, 1996; McEwen et al., 1999; Fink and Anderson, 2000; Carr and Head, 2010). Significant differences in the size of features being compared could account for Tharsis roughness characteristics not aligning closely with terrestrial results.

Another process that degrades lava flows on Mars is impact gardening. Surface impact events crumble the shallow material near the site, and unearth buried strata as part of ejecta blankets (Melosh, 1989; Hartmann et al., 2001). The depth of excavation

depends on the size of the bolide, but even micrometeorite impacts are significant contributors to this process (Maurette, 2006). Impact gardening is the main method of regolith development in planetary environments that lack a thick atmosphere (Neukum et al., 2001; Speyerer et al., 2016) and is active on present-day Mars (Malin et al., 2007).

For these reasons lava surface roughness in the Tharsis region may still show significant differences from the Mauna Ulu and Amboy terrestrial analogue sites. These differences hinder identification based roughness values as the small scale signatures are significantly affected by dust cover, while the large scale features dwarf volcanic landscapes on Earth. However, roughness patterns formed by these values could prove to be useful identification tools.

5.4 Mapping Volcanic Environments using Roughness

Finally, I sought to determine the effectiveness of both the values and patterns produced by TPI and RD methods as means of mapping volcanic features and environments. Based on the results of both methods I conclude that TPI is the better suited for locations with significant regional slope that may impact the roughness results as TPI detrends elevations automatically but the RD method does not. Additionally, TPI successfully identifies large or extensive lava flow features such as flow margins, tumuli several meters in diameter, and lava channels (Figures 16-21). The 10-meter TPI maps of Amboy Crater (Figures 16-19) showed additional, smaller patterns of roughness surrounding the main linear outlines displayed in RD maps of the same scale (Figures 25-28). However, RD efficiently illustrates roughness characteristics at small (less than 10m) scales. Lava features present in the SfM DEMs were more clearly represented by RD results (Figure 23 and 24) than TPI (Figure 14 and 15). Furthermore, RD maps better

display distinctions between lava morphology identified at Obsidian Dome by Anderson et al. (1998) (Figure 22) that are not as clear as with TPI (Figure 13). TPI and RD are appropriate for different scales. Therefore, both methods should be applied to construct the most accurate representation of the volcanic environment.

5.5 Conclusions

This project confirms that suspected basaltic lava flows on Mars fall within the range of roughness values and statistical distributions calculated for basaltic flows at Amboy, California and Mauna Ulu, Hawaii. Additionally, this work also supports the relationship between roughness of small (<10m) lava flow features and emplacement conditions of the flow. I was able to use roughness of lava flows within and outside of the main wind shadow at Amboy to describe the effect of mantling on the lava topography. Though a roughness trend was observed, it is not robust enough to be used as the only method to detect mantled lava flows on Mars. Finally, both the RD and TPI methods can be useful when mapping volcanic environments but both should be applied selectively as each one is most efficient at certain scales.

5.5.1 Further Applications and Recommendations

There is significant research on the links between field measured morphology of lava flow surfaces and emplacement conditions in order to describe past activity, predict the most likely future scenarios, and apply these explanations to planetary environments (Byrnes et al., 2001; Byrnes et al., 2004; Crown and Baloga, 1999; Fink, 1980; Moore et al., 1975; Mallonee et al., 2017). While the trends in RD values presented here are consistent with mantling processes at the Amboy location, this trend is not robust. Therefore, it not reliable enough to conclusively identify mantled surfaces on Mars.

Future work related to this thesis can build on this to develop a tool that decisively detects mantled and uncovered martian lava flows.

Additionally, this technique could potentially be applied to submarine environments on Earth. For example, the Chapopote asphalt volcano in the Gulf of Mexico is a hydrocarbon seep on the ocean floor with notable variation in morphology (Marcon et al., 2018). This marine volcano is not fully understood due to poor resolution of the vent and surrounding asphalt flow fields because of its location on the ocean floor. It is possible to generate high resolution topographic maps from recently collected side-scan sonar data to determine patterns of roughness on the flow surfaces. This could give insight into the processes responsible for forming these flows and provide a better understanding of how this unique volcano works. This project presents an innovative and cost-effective method for understanding the mechanisms of volcanic emplacement that we cannot directly observe.

5.5.2 Improvements to Future Methodology

Any future work that builds on this project should be precise with photo surveys in the field. The method of testing accuracy used by Verma and Bourke (2018) should be practiced in a controlled environment before attempting to image the location, and then repeated briefly in the field to confirm quality. Although the SfM method used in this project is meant to be an affordable, accessible, and high resolution alternative to LiDAR, it could be helpful to have airborne coverage of the selected site to check the precision and accuracy of the SfM DEM.

If Amboy lava flows are revisited, researchers should travel with equipment to measure sand depth at Amboy to complement the estimates of mantling difference at

locations within and outside of the primary wind streak. This would provide a way to quantify the transition between heavily mantled and relatively unmantled areas. To further expand on the comparisons presented in this project, future investigations should include other volcanic compositions, environments and features. Since the Mono-Inyo Craters are briefly compared in this paper, this site would be a logical addition. However, this would result in an even larger dataset of maps and related roughness statistics than the one produced here. Comparing trends and statistical distributions from each additional location and scale will easily overwhelm the human eye, and would likely contribute to interpretation errors if significantly more sites and roughness scales were added. Therefore, it would be highly valuable to consider the method of machine learning and self-organizing maps utilized by Burzynski et al. (2018) to compare thermal patterns of the lava lake at Kilauea volcano to eruption conditions using thermal photographs of the lake taken over a span of years.

REFERENCES

Agisoft LLC, 2018, Agisoft Metashape User Manual: Professional Edition, v. 1.5

Anderson, S.W., and Fink, J. H., 1989, Hydrogen-isotope evidence for extrusion mechanisms of the Mount St Helens lava dome: Nature, v.341, p.521.

Anderson, S.W., and Fink, J.H., 1992, Crease structures as indicators of emplacement rates and surface stress regimes of lava flows: Geological Society of America Bulletin, v. 104, p. 615–626.

Anderson, S. W., Fink, J. H., and Rose, W. I., 1995, Mount St. Helens and Santiaguito lava domes: The effect of shortterm eruption rate on surface texture and degassing processes: Journal of Volcanology and Geothermal Research, v. 69, p. 105–116.

Anderson, S.W., Stofan, E.R., Plaut, J.J., and Crown, D.A., 1998, Block size distributions on silicic lava flow surfaces: Implications for emplacement conditions: Geological Society of America Bulletin, v.110, p.1258-1267.

Anderson, S.W., Smrekar, S.E., and Stofan, E.R., 2012, Tumulus development on lava flows: insights from observations of active tumuli and analysis for formation models: Bulletin of Volcanology, v. 74, p. 931-946.

Bleacher, J. E., Greeley, R., Williams, D. A., Cave, S. R., and Neukum, G., 2007, Trends in effusive style at the Tharsis Montes, Mars, and implications for the development of the Tharsis province: Journal of Geophysical Research: Planets, v. 112.

Bonatti, E., and Harrison, C.G.A., 1988, Eruption styles of basalt in oceanic spreading ridges and seamounts: Effect of magma temperature and viscosity: Journal of Geophysical Research, v.93, p. 2967-2980.

Booth, A. M., Roering, J. J., and Perron, J. T., 2009, Automated landslide mapping using spectral analysis and high-resolution topographic data: Puget Sound lowlands, Washington, and Portland Hills, Oregon: Geomorphology v. 109, p. 132–147.

Brasington, J., Vericat, D., and Rychkov, I., 2012, Modeling river bed morphology, roughness, and surface sedimentology using high resolution terrestrial laser scanning: Water Resources Research, v 48.

Bretar, F., Arab-Sedze, M., Champion, J., Pierrot-Deseilligny, M., Heggy, E., and Jacquemoud, S., 2013, An advanced photogrammetric method to measure surface roughness: Application to volcanic terrains in the Piton de la Fournaise, Reunion Island: Remote Sensing of the Environment, v. 135, p. 1-11.

Brown, S. R., and C. H. Scholz, 1985, Broad bandwidth study of the topography of natural rock surfaces: Journal of Geophysical Research, v.90, p.575-582.

Brož, P., Hauber, E., Wray, J.J. and Michael, G., 2017, Amazonian volcanism inside Valles Marineris on Mars: Earth and Planetary Science Letters, v. 473, p. 122-130.

Burzynski, A., 2015, Lava lake thermal pattern classification using self-organizing maps and relationships to eruption processes at Kilauea Volcano, Hawai'i [Master thesis]: University of Northern Colorado, 95 p.

Byrnes, J.M., and Crown, D.A., 2001, Relationships between pahoehoe surface units, topography and lava tubes at Mauna Ulu, Kilauea Volcano, Hawaii: Journal of Geophysical Research, v.106, p.2139–2151.

Byrnes, J.M. and Crown, D. A., 2002, Morphology, stratigraphy, and surface roughness properties of Venusian lava flow fields: Journal of Geothermal Research, v. 107, p. 5079.

Byrnes, J. M., Ramsey, M. S., and Crown, D. A., 2004, Surface unit characterization of the Mauna Ulu flow field, Kilauea Volcano, Hawai'i, using integrated field and remote sensing analyses: Journal of Volcanology and Geothermal Research, v 135, p. 169-193.

Bywater-Reyes, S., Segura, C., Bladon, K. D., 2017, Geology and geomorphology control suspended sediment yield and modulate increases following timber harvest in temperate headwater: Journal of Hydrology, v.548, p.754-769.

Campbell, B.A., and Shepard, M.K., 1996, Lava flow surface roughness and depolarized radar scattering: Journal of Geophysical Research, v. 101, p. 941-951.

Carr, M. H., and Head, J. W., 2010, Geologic history of Mars: Earth and Planetary Science Letters, v. 294, p.185-203.

Cervantes, P., and Wallace, P., 2003, Magma degassing and basaltic eruption styles: a case study of ~2000 year BP Xitle volcano in central Mexico: Journal of Volcanology and Geothermal Research, v.120, p.249-270.

Chapman, W. H., 1985, Aerial Profiling of Terrain System (APTS) applications test report-Charles River Project: U.S. Geologic Survey Open File Report.

Chesterman, C. W., 1971, Volcanism in California: California Geology, v. 24, p. 139-147.

Christensen, P. R., Bandfield, J. L., Smith, M. D., Hamilton, V. E., and Clark, R. N., 2000, Identification of a basaltic component on the Martian surface from Thermal Emission Spectrometer data: Journal of Geophysical Research: Planets, v. 105(E4), p. 9609-9621.

Craddock, R.A., and Howard, A.D., 2002, The case for rainfall on a warm, wet early Mars: Journal of Geophysical Research, v. 107, p. 1–36.

Crown, D. A., Berman, D. C., and Ramsey, M. S., 2015, Lava flow fields of Southern Tharsis, Mars: Flow types, interactions, and ages: Proceedings from the 46th Lunar and Planetary Science Conference in Houston, Texas.

Crown, D.A., and Baloga, S.M., 1999, Pahoehoe toe dimensions, morphology, and branching relationships at Mauna Ulu, Kilauea Volcano, Hawai'i: Bulletin of Volcanology, v. 61, p. 288-305.

Csárdi, G., Wickham, H., Chang, W., Hester, J., Morgan, M., and Tenenbaum, D., 2018, Remotes: R Package Installation from Remote Repositories, Including 'GitHub'. R package v. 2.0.2, https://CRAN.R-project.org/package=remotes.

Deeb, E. J., and LeWinter, A. L., 2018, Building Envelope Assessment Using Thermal Infrared and Lidar Scanning: Palmer Station, Antarctica (No. ERDC/CRREL-TR-18-9). Engineer Research and Development Center HANOVER.

Diniega, S., Sangha, S., and Browne, B., 2018, Using satellite imagery to identify and analyze tumuli on Earth and Mars: Earth and Planetary Science Letters, v. 482, p. 52-61.

Drake, J., Dubayah, R., Clark, D., Knox, R., Blair, J., Hofton, M., Chazdon, R., Weishampel, J., Prince, S., 2002. Estimation of tropical forest structural characteristics using large-footprint lidar: Remote Sensing of Environment, v. 79, p. 305-319.

Evans, D. L., Farr, T. G., and Van Zyl, J. J., 1992, Estimates of surface roughness derived from synthetic aperture radar (SAR) data: IEEE Transactions on Geoscience and Remote sensing, v. 30, p. 382-389.

Fan K.A., Neish, C. D., Zanetti, M., and Kukko, A., 2018, An improved methodology for the 3-dimensional characterization of surface roughness as applied to lava flows: Houston, Texas, Lunar and Planetary Science Conference LXIX abstract #2526.

Farr T. G., 1992, Microtopographic Evolution of Lava Flows at Cima Volcanic Field, Mojave Desert, California: Journal of Geophysical Research, v. 97, n. Bll, p 15,171-15,179.

Farr, T. G., and Engheta, N., 1983, Quantitative comparisons of radar image, scatterometer, and surface roughness data from Pisgah Crater, CA.: San Francisco, California, International Geoscience Remote Sensing Symposium, 2.1–2.6.

Favalli M, Fornaciai A, Isola I, et al. (2012) Multiview 3D reconstruction in geosciences. Computers & Geosciences 44: 168–176.

Fidera, A., Chapman, M., and Hong, J., 2004, Terrestrial lidar for industrial metrology applications: Modelling, enhancement and reconstruction: International Archives of Photogrammetry, Remote Sensing and Spatial Information Sciences, v. 35 (Part B5), p. 880-883.

Fink, J. F., 1980, Surface folding and viscosity of rhyolite flows: Geology, v. 8, p. 250-254.

Fink, J.H., and Grifiths, R.W., 1998, Morphology, eruption rates, and rheology of lava domes: insights from laboratory models: Journal of Geophysical Research, v.103, p.527–546.

Fink J. H. and Anderson S. W., 2000, Lava Domes and Coulees *in* Sigurdsson, H., Houghton, B.F., McNutt, S.R., Rymer, H., and Stix, J., et al., Encyclopedia of Volcanoes: Academic Press, San Diego, v. 1, p. 307-320.

Finnegan D. C., Ghent, R.R., Byrnes, J.M. and Bourke, M.C., 2004, Morphometric LIDAR analysis of Amboy crater, California: Application to MOLA analysis of analog features on Mars: Houston, Texas, Lunar and Planetary Science Conference XXXV, abstract #1736.

Finnerty, A. A., Phillips, R. J., and Banerdt, W. B., 1988, Igneous processes and closed system evolution of the Tharsis region of Mars: Journal of Geophysical Research: Solid Earth, v. 93, p. 10225-10235.

Gaddis, L. R., Mouginis-Mark, P. J., and Hayashi, J. N., 1990, Lava flow surface textues: SIR-Bradar image texture, field observations and terrain measurements: Photogrammetric Engineering and Remote Sensing, v. 56, p. 211-224.

Garfunkel, Z., 1974, Model for the Late Cenozoic Tectonic History of the Mojave Desert, California, and for its relation to adjacent regions: GSA Bulletin, v. 85, p. 12.

Garneau, S., and Plaut, J. J., 2000, Topographic and roughness characteristics of the Vastitas Borealis formation on Mars described by fractal statistics. Houston, Texas, Lunar and Planetary Science Conference XXXI, abstract, 1115.

Giacomini, L., Massironi, M., Martellato, E., Pasquarè, G., Frigeri, A., and Cremonese, G., 2009, Inflated flows on Daedalia Planum (Mars)? Clues from a comparative analysis with the Payen volcanic complex (Argentina): Planetary Space Science v.57, p. 556–570.

Glaze, L.S., Anderson, S.W., Stofan, E.R., Baloga, S., and Smrekar, S.E., 2005, Statistical distribution of tumuli on pahoehoe flow surfaces: Analysis of examples in Hawaii and Iceland and potential applications to lava flows on Mars: Journal of Geophysical Research, v.110, p.B08202.

Glazner, A. F., Farmer, G. L., Hughes, W. T., Wooden, J. L., and Pickthorn, W., 1991, Contamination of basaltic magma by mafic crust at Amboy and Pisgah Craters, Mojave Desert, California: Journal of Geophysical Research: Solid Earth, v.96, issue B8, doi.org/10.1029/91JB00175

Golombek, M. P., Cook, R. A., Moore, H. J., and Parker, T. J., 1997, Selection of the Mars Pathfinder landing site: Journal of Geophysical Research: Planets, v. 102, p. 3967-3988.

Google Inc., 2015, Google Earth, v. 6.1.0.5001, software available from http://www.google.com/earth

Greeley, R. and Bunch, T. E., 1976, basalt models for the Mars penetrator mission: geology of the Amboy lava field, California: NASA technical memorandum.

Greeley, R., and Martel, L., 1988, Radar observations of basaltic lava flows: International Journal of Remote Sensing, v. 9, p. 1071-1085.

Greeley, R., Lancaster, N., Sullivan, R. J., Saunders, R. S., Theilig, E., Wall, S., Dobrovolskis, A., White, B. R., and Iversen, J. D., 1998, A relationship between radar backscatter and aerodynamic roughness: preliminary results: Geophysical Research Letters, v.5, p.565–568.

Gregg, T.K.P., and Fink, J.H., 1995, Quantification of submarine lava flow morphology through analog experiments: Geology, v.23, p.73–76

Guest, J., Duncan, A., Stofan, E.R., and Anderson, S.W., 2011, Effect of slope on development of pahoehoe flow fields: Evidence from Mount Etna: Journal of Volcanology and Geothermal Research, v. 219–220, p. 52-62.

Halliday, A. N., Wänke, H., Birck, J. L., and Clayton, R. N., 2001, The accretion, composition and early differentiation of Mars: Space Science Reviews, v. 96, v. 197-230.

Hamilton, C.W., Mouginis-Mark, P.J., Sori, M.M., Scheidt, S.P., and Bramson, A.M., 2018, Episodes of aqueous flooding and effusive volcanism associated with Hrad Vallis, Mars: Journal of Geophysical Research Planets, v.123, p.1484-1510

Hauber E., Brož P., Jagert F., Jodłowski P., and Platz T., 2011, Very recent and wide-spread basaltic volcanism on Mars: Geophysical Research Letters, v.38, E12S43.

Head, J. W., Crumpler, L. S., Aubele, J. C., Guest, J. E., and Saunders, R. S., 1992, Venus volcanism: Classification of volcanic features and structures, associations, and global distribution from Magellan data: Journal of Geophysical Research: Planets, v. 97, p. 13153-13197.

Head J.W., Wilson L., Dickson J., and Neukum G., 2006, The Huygens-Hellas giant dike system on Mars: implications for Late Noachian–Early Hesperian volcanic resurfacing and climatic evolution: Geology v.34 p. 285–288.

Hodgson, M. E., and Bresnahan, P., 2004, Accuracy of Airborne Lidar-Derived Elevation: Empirical Assessment and Error Budget: Photogrammetric Engineering & Remote Sensing, v. 70, p. 331–339.

Huges, S.S., Haberle, C.W., Kobs Nawotniak, S.E., Sehlke, A., Garry, W.B., Elphic, R.C., Payler, S.J., Stevens, A.H., Cockell, C.S., Brady, A.L., Heldmann, J.L., Lim, D.S.S., 2019, Basaltic terrains in Idaho and Hawai‘i as planetary analogs for Mars geology and astrobiology: Astrobiology, v. 19.

Irish, J., and Lillycrop, W., 1999, Scanning laser mapping of the coastal zone: The SHOALS system: ISPRS Journal of Photogrammetry & Remote Sensing, v. 54, p. 123- 129.

James, M. R., and Robson, S., 2012, Straightforward reconstruction of 3D surfaces and topography with a camera: Accuracy and geoscience application: Journal of Geophysical Research: Earth Surface, v. 117, p. F03017.

Javernick, L., Brasington, J., and Caruso, B., 2014, Modelling the topography of shallow braided rivers using Structure from Motion photogrammetry: Geomorphology, v 213, p. 166–182.

Jenness, J., 2006, Topographic Position Index (tpi_jen.avx) extension for ArcView 3.x, v. 1.2. Jenness Enterprises. Available at: http://www.jennessent.com/arcview/tpi.htm.

Jutzi, B., and Stilla, U., 2003, Laser pulse analysis for reconstruction and classification of urban objects: International Archives of Photogrammetry, Remote Sensing and Spatial Information Sciences v. 34 (Part 3/W8), p. 151-156.

Keszthelyi, L., Jaeger, W., McEwen, A., Tornabene, L., Beyer, R. A., Dundas, C., and Milazzo, M., 2008, High Resolution Imaging Science Experiment (HiRISE) images of volcanic terrains from the first 6 months of the Mars Reconnaissance Orbiter primary science phase: Journal of Geophysical Research: Planets, v. 113 p. E4.

Kienenberger, R. L. and Greeley, R., 2012, Field analog studies of the distribution of wind blown sediments at Amboy Crater, California, with application to Mars: Planetary and Space Science v. 68, p. 25–33.

Kilburn, C.R.J., 1981, Pahoehoe and aa lavas: a discussion and continuation of the model of Peterson and Tilling: Journal of Volcanology and Geothermal Research, v.11, p.373–389.

Kim J. R. and Muller J. P, 2008, International Archives of Photogrammetry, Remote Sensing and Spatial Information Science XXXVII p. 993-998.

Kirk, R. L., Howington-Kraus, E., Rosiek, M. R., Anderson, J. A., Archinal, B. A., Becker, K. J., Holmberg, I. M et al., 2008, Ultrahigh resolution topographic mapping of Mars with MRO HiRISE stereo images: Meter-scale slopes of candidate Phoenix landing sites: Journal of Geophysical Research: Planets, v. 113.

Kreslavsky, M. A., and Head, J. W., 2000, Kilometer-scale roughness of Mars: Results from MOLA data analysis: Journal of Geophysical Research: Planets, v. 105, p. 26695-26711.

Lang, N. P., Tornabene, L. L., McSween Jr, H. Y., & Christensen, P. R., 2009, Tharsis-sourced relatively dust-free lavas and their possible relationship to Martian meteorites: Journal of Volcanology and Geothermal Research, v. 185, p. 103-115.

Lefsky, M., Cohen, W., Acker, S., Parker, G., Spies, T., and Harding, D., 1999, Lidar remote sensing of the canopy structure and biophysical properties of Douglas fir western hemlock forests: Remote Sensing of Environment, v. 70, p. 339-361.

Li, R., Hwangbo, J., Chen, Y., and Di, K., 2011, Rigorous photogrammetric processing of HiRISE stereo imagery for Mars topographic mapping: IEEE Transactions on Geoscience and Remote Sensing, v. 49(7), p. 2558-2572.

Long, P. E., and Wood, B. J., 1986, Structures, textures, and cooling histories of Columbia River basalt flows: Geological Society of America Bulletin, v. 97, p. 1144-1155.

Lopes, R. M. C., and Kilburn, C. R. J., 1990, Emplacement of lava flow fields: Application of terrestrial studies to Alba Patera, Mars: Journal of Geophysical Research, v. 95, p. 383–397.

Malin, M. C., Bell, J. F., Cantor, B. A., Caplinger, M. A., Calvin, W. M., Clancy, R. T., Lee, S. W., et al., 2007, Context camera investigation on board the Mars Reconnaissance Orbiter: Journal of Geophysical Research: Planets, v. 112.

Mallonee H. C., Nawotniak, S. E. K., McGregor, M., Hughes S. S., Neish, C. D., Downs, M., Delparte, D., Lim, D. S. S., and Heldmann J., 2017, Lava flow morphology classification based on measures of roughness: Houston, Texas, Lunar and Planetary Science Conference XLVIII, abstract #2992.

Mallonee, H.C., Nawotniak, S. E. K., McGregor, M., Hughes S. S., Neish, C. D., Downs, M., Delparte, D., Lim, D. S. S., and the FINESSE, 2017, Lava Texture Classification as a Function of Scale for RMS Height and Area Ratio Methods: Houston, Texas, Lunar and Planetary Science Conference XLVIII, abstract #2975.

Marcon, Y., Sahling, H., MacDonald, I. R., Wintersteller, P., dos Santos Ferreira, C., and Bohrmann, G., 2018, Slow volcanoes: The intriguing similarities between marine asphalt and basalt lavas: Oceanography, v. 31, p. 2.

Maurette, M., 2006, Micrometeorites and the mysteries of our origins p. 54-71.

McCue, G. A., and J. Green, 1965, Pisgah Crater terrain analysis: Photogrammetry Engineering, v. 31, p. 810-821.

McEwen, A.S., Malin, M.C., Carr, M.H., and Hartmann, W.K., 1999, Voluminous volcanism on early Mars revealed in Valles Marineris: Nature, v. 397, p. 584–586.

McEwen, A. S., Eliason, E. M., Bergstrom, J. W., Bridges, N. T., Hansen, C. J., Delamere, W. A., Kirk, R. L., et al., 2007, Mars reconnaissance orbiter's high resolution imaging science experiment (HiRISE): Journal of Geophysical Research: Planets, v. 112.

McSween, H.Y., Grove, T.L., and Wyatt, M. B., 2003, Constaints on the composition and petrogenesis of the Martian crust: Journal of Geophysical Research, v. 108, doi:10.1029/2003JE002175.

Mege, D., and Masson, P., 1996, A plume tectonics model for the Tharsis province, Mars: Planetary Space Science v. 44, p. 1499–1546.

Melosh, H. J.,1989, Impact cratering: A geologic process *in* Oxford Monographs on Geology and Geophysics, New York, Oxford University Press, v. 253 p. 11.

Micheletti, N., Chandler, J.H. and Lane, S.N., 2015. Structure from motion (SFM) photogrammetry, *in*: Clarke, L.E. and Nield, J.M. (Eds.) Geomorphological

Techniques (Online Edition). London: British Society for Geomorphology. ISSN: 2047-0371, Chap. 2, Sec. 2.2.

Moncrief S. R. and Rowland S. K., 1991, Analysis of Hawaiian lava surface roughness with Thermal Infrared Images: Houston, Texas, Lunar and Planetary Science Conference XXII program, p. 913-914.

Moore, J.G., Phillips, R.L., Grigg, R.W., Peterson, D.W., and Swanson, D.A., 1975, Flow of lava into the sea, 1969-1971, Kilauea Volcano, Hawaii: Geological Society of America Bulletin, v. 84, p. 537-546.

Morris, A. R., Anderson, F. S., Mouginis-Mark, P. J., Haldemann, A. F. C., Brooks, B. A., and Foster, J., 2008, Roughness of Hawiian volcanic terrains: Journal of Geophysical Research, v. 113, p. E12007.

Neukum, G., Ivanov, B. A. & Hartmann, W. K., 2001, Cratering records in the inner Solar System in relation to the lunar reference system: Space Science Review v. 96, p. 55–86.

Newsom, H. E., Crumpler, L. S., Reedy, R. C., Petersen, M. T., Newsom, G. C., Evans, L. G., and Kerry, K., 2007, Geochemistry of Martian soil and bedrock in mantled and less mantled terrains with gamma ray data from Mars Odyssey: Journal of Geophysical Research: Planets, v. 112, p. E3.

Parfitt, E.A., 2004, A discussion of the mechanisms of explosive basaltic eruptions: Journal of Volcanology and Geothermal Research, v.134, p.77-107.

Peterson, D.W., and Tilling, R.I., 1980, Transition of basaltic lava from pahoehoe to aa, Kilauea Volcano, Hawaii: Field observations and key factors: Journal of Volcanology and Geothermal Research, v. 7, p. 271-293.

Phillips, F. M., 2003, Cosmogenic 36Cl ages of Quaternary basalt flows in the Mojave Desert, California, USA: Geomorphology, v. 53, p. 199-208.

Plaut, J. J., Stofan, E. R., Crown, D. A., and Anderson, S. W., 1994, Topographic and surface roughness properties of steep-sided domes on Venus and Earth from radar remote sensing and field measurements: Houston, Texas, Lunar and Planetary Science Conference XXV, v. 3, p. 1091–1092.

Plaut, J. J., Anderson, S. W., Crown, D. A., Stofan, E. R., and van Zyl, J.J., 2002, The unique radar properties of silicic lava domes: Journal of Geophysical Research, v.109, E03001.

R Core Team, 2018, R: A language and environment for statistical computing. R Foundation for Statistical Computing, Vienna, Austria, https://www.R-project.org/.

Ramsey, M. S., and Fink, J. H., 1999, Estimating silicic lava vesicularity with thermal remote sensing: A new technique for volcanic mapping and monitoring: Bulletin of Volcanology, v. 61, p. 32-39.

Rychkov, I., Brasington, J., and Vericat, D., 2012, Computational and methodological aspects of terrestrial surface analysis based on point clouds: Computers and Geosciences, v.42, p. 64-70.

Schon, S. C., Head, J. W., and Fassett, C. I., 2012, Recent high-latitude resurfacing by a climate-related latitude-dependent mantle: Constraining age of emplacement from counts of small craters: Planetary and Space Science, v. 69(1), p. 49-61.

Shepard, M.K., Campbell, B.A., Bulmer, M.H., Farr, T.J., Gaddis, L.R., and Plaut, J.J., 2001, The roughness of natural terrain: A planetary and remote sensing perspective: Journal of Geophysical Research, v. 106, p. 32.

Simurda C.M., 2018, Modeling particle size distributions that cause the unique thermophysical variations in Daedalia Planum, Mars: Houston, Texas, Lunar and Planetary Science Conference LXIX, abstract #2612.

Sithole, G., and Vosselman, G., 2006, Bridge detection in airborne laser scanner data: ISPRS Journal of Photogrammetry & Remote Sensing, v. 61, p. 33-46.

Smith, M. W., Carrivick, J. L., and Quincy, D. J., 2016, Structure from motion photogrammetry in physical geography: Progress in Physical Geography, v. 40(2), p. 247–275

Smith, M.W., 2014, Roughness in the Earth Sciences: Earth-Science Reviews, v. 136, p. 202-225.

Solomon, S. C. and Head, J. W., 1982, Evolution of the Tharsis Province of Mars: The Importance of Heterogeneous Lithospheric Thickness and Volcanic Construction: Journal of Geophysical Reseach v. 87: p. 9755–9774.

Speyerer, E. J., Povilaitis, R. Z., Robinson, M. S., Thomas, P. C., and Wagner, R. V., 2016, Quantifying crater production and regolith overturn on the Moon with temporal imaging: Nature, v. 583, p. 215-218.

Stofan, E. R., Anderson, S. W., Crown, D. A., and Plaut, J. J., 2000, Emplacement and composition of steep-sided domes on Venus: Journal of Geophysical Research, v. 105, p. 757-771.

Swanson, D.A., 1973, Pahoehoe Flows from the 1969-1971 Mauna Ulu Eruption, Kilauea Volcano, Hawaii: Geological Society of America Bulletin, v. 84, p. 615-626.

Tanaka, K. L., 2000, Dust and ice deposition in the Martian geologic record: Icarus, v. 144(2), p. 254-266.

Theilig E. and Greeley R., 1986, Lava flows on Mars: Analysis of small surface features and comparisons with terrestrial analogs: Journal of Geothermal Research, v.91, p. 193-206.

Theilig, E., Wall, S., and Saunders, R. S., 1988, Radar interpretation of lava fields as a function of incidence angle – implications for interpretation of Magellan SAR data on Venus: Houston, Texas, Lunar and Planetary Science Conference XIX, abstract #1591.

Tian, B., Wang, L., and Koike, K., 2011, Spatial statistics of surface roughness change derived from multi-scale digital elevation models: Procedia Environmental Sciences, v. 7, p. 252-257.

Tolometti G. D., Neish C. D., Osinski, G. R., Zanetti, M., Maj, R., Hughes, S. S., and Nawotniak, S. E. K, 2017, Variation in petrography of basaltic lava flows with similar surface roughness Houston, Texas, Lunar and Planetary Science Conference XLVIII abstract #1643.

Verma, A. K., and Bourke, M. C., 2018, A Structure from Motion photogrammetry-based method to generate sub-millimetre resolution Digital Elevation Models for investigating rock breakdown features: Earth Surface Dynamics Discussions, v. 7,

Vu, V. Q., 2011, ggbiplot: A ggplot2 based biplot. R package v. 0.55, http://github.com/vqv/ggbiplot

Ward, A. W., 1979, Yardangs on Mars: Evidence of recent wind erosion: Journal of Geophysical Research: Solid Earth, v. 84(B14), p. 8147-8166.

Watters, T. R., 1991, Origin of periodically spaced wrinkle ridges on the Tharsis Plateau of Mars: Journal of Geophysical Research: Planets, v. 96, p. 15599-15616.

Weiss, A. D., 2001, Topographic Position and Landform Analysis: Proceedings, ESRI User Conference, San Diego, CA, v. 200.

Wells, S. G., Dohrenwend, J. C., McFadden, L. D., Turrin, B. D., and Mahrer, K. D., 1985, Late Cenozoic landscape evolution on lava flow surfaces of the Cima volcanic field, Mojave Desert, California: Geological Society of America Bulletin, v. 96, p. 1518-1529.

Werner, S. C., 2009, The global martian volcanic evolutionary history: Icarus, v.201, p. 44–68.

Westoby, M. J., Brasington, J., Glasser, N. F., Hambrey, M. J., and Reynolds, J.M., 2012, 'Structure-from-Motion' photogrammetry: a low-cost, effective tool for geoscience applications: Geomorphology, v. 179, p. 300-314.

Whelley, P. L., Glaze, L. S., Clader, E. S., and Harding, D. J., 2014, LiDAR-Derived Surface Roughness Texture Mapping: Application to Mount St. Helens Pumice Plain Deposit Analysis: IEEE Transactions on Geoscience and Remote Sensing, v. 52, p. 426-438.

Wise, D.U., Golombek, M. P., and McGill, G. E., 1979, Tharsis province of Mars: Geologic sequence, geometry, and a deformation mechanism: Icarus, v. 38, p. 456–472

Zanetti M., Neish C. D., Kukko, A., Choe, B. –H., Osinski, G. R., Tolometti, G. D., Fan , K.A., Maj, R., and Heldmann J., 2018, Surface roughness and radar scattering properties of volcanic terrain: geologic application of kinematic mobile LiDAR scanning: Houston, Texas, Lunar and Planetary Science Conference LXIX abstract #2361.

APPENDIX

R CODE FOR PRINCIPAL COMPONENT ANALYSIS

Example of how to run the PCA:

Import dataset to R. Data must be in .txt format.

```
      > setwd("E:/thesis files")
> mantling <- read.table("Mantling.txt", header=TRUE)
> View(mantling)
> mantling.pca <- prcomp(mantling, center = TRUE, scale = TRUE)
> summary(mantling.pca)
Importance of components:
                          PC1    PC2    PC3     PC4     PC5    PC6
      PC7     PC8    PC9
Standard deviation     2.6589 1.9471 1.6864 1.30980 0.95038 0.8970
      0.68822 0.52680 0.2546
Proportion of Variance 0.3928 0.2106 0.1580 0.09531 0.05018 0.0447
      0.02631 0.01542 0.0036
Cumulative Proportion  0.3928 0.6034 0.7614 0.85671 0.90689 0.9516
      0.97790 0.99332 0.9969
                          PC10    PC11    PC12    PC13     PC14
      PC15      PC16
Standard deviation     0.21354 0.08817 0.03423 0.02846 0.009132
      0.001605 9.993e-17
Proportion of Variance 0.00253 0.00043 0.00007 0.00004 0.000000
      0.000000 0.000e+00
Cumulative Proportion  0.99945 0.99989 0.99995 1.00000 1.000000
      1.000000 1.000e+00
```

#Proportion of variance is the percentage of variety in the dataset that this PC explains.

Example of graphing PCA results:

```
library(remotes)
library(ggbiplot)
ggbiplot(mantling.pca)
ggbiplot(mantling.pca, labels=rownames(mantling))
```

#The line of code below labels points on the biplot. The numbers are the number of rows in the table, starting from the top. This labels the points by location and groups them with ellipses.

```
mantling.sites <- c(rep("Amboy", 8), rep("Mars",4), rep("Mauna Ulu",2),
      rep("Inyo", 2))

ggbiplot(mantling.pca, ellipse=TRUE,  labels=rownames(mantling),
      groups=mantling.sites)
```

#This labels the points by scale of observation.

```
mantling.scales <- c(rep("1m",1), rep("10m",1), rep("1m",1),
      rep("10m",1), rep("1m",1),rep("10m",1), rep("1m",1),
      rep("10m",1), rep("1m",1), rep("10m",1),
      rep("1m",1),rep("10m",1), rep("1m",1), rep("10m",1),
      rep("1m",1),rep("10m",1))
ggbiplot(mantling.pca, ellipse=TRUE,  labels=rownames(mantling),
      groups=mantling.scales)
```

A more detailed guide can be found on

https://www.datacamp.com/community/tutorials/pca-analysis-r